Atmos. Chem. Phys., 18, 15535–15553, 2018
https://doi.org/10.5194/acp-18-15535-2018

Atmospheric Chemistry and Physics
Open Access
EGU

Chlorine-initiated oxidation of *n*-alkanes under high-NO_x conditions: insights into secondary organic aerosol composition and volatility using a FIGAERO–CIMS

Dongyu S. Wang and Lea Hildebrandt Ruiz

McKetta Department of Chemical Engineering, The University of Texas at Austin, Austin, TX 78712, USA

Correspondence: Lea Hildebrandt Ruiz (lhr@che.utexas.edu)

Received: 3 May 2018 – Discussion started: 15 May 2018
Revised: 27 September 2018 – Accepted: 29 September 2018 – Published: 30 October 2018

Abstract. Chlorine-initiated oxidation of *n*-alkanes (C_{8-12}) under high-nitrogen oxide conditions was investigated. Observed secondary organic aerosol yields (0.16 to 1.65) are higher than those for OH-initiated oxidation of C_{8-12} alkanes (0.04 to 0.35). A high-resolution time-of-flight chemical ionization mass spectrometer coupled to a Filter Inlet for Gases and AEROsols (FIGAERO–CIMS) was used to characterize the gas- and particle-phase molecular composition. Chlorinated organics were observed, which likely originated from chlorine addition to the double bond present on the heterogeneously produced dihydrofurans. A two-dimensional thermogram representation was developed to visualize the composition and relative volatility of organic aerosol components using unit-mass resolution data. Evidence of oligomer formation and thermal decomposition was observed. Aerosol yield and oligomer formation were suppressed under humid conditions (35 % to 67 % RH) relative to dry conditions (under 5 % RH). The temperature at peak desorption signal, T_{max}, a proxy for aerosol volatility, was shown to change with aerosol filter loading, which should be constrained when evaluating aerosol volatilities using the FIGAERO–CIMS. Results suggest that long-chain anthropogenic alkanes could contribute significantly to ambient aerosol loading over their atmospheric lifetime.

1 Introduction

Alkanes account for up to 90 % of all anthropogenic hydrocarbon emissions and 12 % (140 Tg yr^{-1}) of annual nonmethane hydrocarbon emissions (Fraser et al., 1997; Goldstein and Galbally, 2007; Guenther et al., 2012; Rogge et al., 1993; Schauer et al., 1999, 2002). Alkanes and aromatics are major components of gasoline, diesel, motor oil, and other petroleum products (Caravaggio et al., 2007; Kleeman et al., 2008; Schauer et al., 1999). Depending on its vapor pressure, the alkane can be emitted as volatile organic compound (VOC), intermediate-volatility organic compound, semivolatile organic compound, or primary organic aerosol (POA). Evaporation of POA due to dilution can provide additional gas-phase alkanes, which can undergo photooxidation initiated by OH and NO_3, as well as chlorine radicals (Aschmann and Atkinson, 1995; Atkinson and Arey, 2003). Consequently, alkanes can have significant contributions to SOA production in urban environments (Dunmore et al., 2015). Hydrocarbon-like organic aerosol, which is often associated with POA and alkane oxidation, contributes on average 36 % to fine particulate matter (PM_1) in urban environments (Zhang et al., 2007). Influences of alkane emission and oxidation on SOA formation can be observed in remote regions as well (Carlton et al., 2010; Chrit et al., 2017; Hoyle et al., 2011; Minguillón et al., 2011, 2016; Patokoski et al., 2014; Saito et al., 2004; Sartelet et al., 2012). Alkane emissions can be sporadic and scattered, complicating both monitoring and modeling efforts (Lyon et al., 2015; Zavala-Araiza et al., 2015, 2017). Using laboratory results on OH-initiated SOA formation from alkanes under low- and high-NO_x conditions (Jordan et al., 2008; Lamkaddam et al., 2017; Lim and Ziemann, 2009a, 2005, 2009b; Loza et al., 2014; Presto et al., 2009, 2010; Schilling Fahnestock et al., 2015; Takekawa et al., 2003; Tkacik et al., 2012; Yee et al., 2012, 2013; Zhang et al., 2014), model predictions for OA concentrations can be improved, though the predicated OA is often less oxidized

than observed (Bahreini et al., 2012; DeCarlo et al., 2010; Dzepina et al., 2009; de Gouw et al., 2011; Murphy and Pandis, 2009; Shrivastava et al., 2008; Zhang et al., 2007), which could point to missing oxidants (e.g., Cl) and SOA oxidation mechanisms in the models (Murphy and Pandis, 2009).

Recent field studies have identified reactive chlorine compounds in diverse locales from natural and anthropogenic sources (Faxon and Allen, 2013; Finlayson-Pitts, 2010; Saiz-Lopez and von Glasow, 2012; Simpson et al., 2015). Tropospheric chlorine chemistry can enhance ozone production (Tanaka et al., 2003). Night-time production of nitryl chloride mediated by heterogeneous uptake of NO_x onto chloride-containing particles represents an ubiquitous source of reactive chlorine (Thornton et al., 2010). In addition, biomass burning could also act as a source of $ClNO_2$ (Ahern et al., 2018). $ClNO_2$ photolysis in the early morning produces Cl and NO_x, which has been shown to enhance RO_2 production from alkane oxidation near coastal regions (Riedel et al., 2012) as well as OH radical propagation in urban environments (Young et al., 2014). In addition to reactive chlorine emissions from water treatment (Chang et al., 2001) and fuel combustion (Osthoff et al., 2008; Parrish et al., 2009), the rising usage of volatile chemical products such as pesticides, cleaning products, and personal care products may be a significant source of reactive chlorine compounds and VOCs in urban environments (Khare and Gentner, 2018; McDonald et al., 2018). VOC-Cl oxidation products such as isomers of 1-chloro-3-methyl-3-butene-2-one, a tracer for isoprene–Cl chemistry (Nordmeyer et al., 1997), have been observed in highly polluted environments (Le Breton et al., 2018; Tanaka et al., 2003).

Akin to OH radicals, Cl radicals initiate reactions with alkanes via hydrogen abstraction, forming hydrogen chloride (HCl) and alkylperoxy radicals (RO_2). According to structure–activity relationships, terminal hydrogen abstraction occurs more frequently with alkane–Cl than with alkane–OH reactions (Kwok and Atkinson, 1995), resulting in different product distributions, for example increased formation of primary alkyl nitrates. The biomolecular gas-phase reaction rate constants with linear alkanes for OH radicals and Cl radicals increase with the alkane chain length. Consequently, the reaction rate constants for Cl and linear C_{8-12} alkanes range from 4.05×10^{-10} (octane) to 5.36×10^{-10} cm^{-3} $molecules^{-1}$ s^{-1} (dodecane) at 298 K and 1 atm (Aschmann and Atkinson, 1995), which is over an order of magnitude higher than the rate constants for OH radicals, 8.11×10^{-12} (octane) to 1.32×10^{-11} cm^{-3} $molecules^{-1}$ s^{-1} (dodecane; Atkinson and Arey, 2003). Studies show that Cl-initiated oxidation of volatile organic compounds such as isoprene, monoterpenes, toluene, and polycyclic aromatic hydrocarbons can lead to rapid SOA formation with high yields (Cai et al., 2008; Cai and Griffin, 2006; Huang et al., 2014; Karlsson et al., 2001; Ofner et al., 2013; Riva et al., 2015; Wang and Hildebrandt Ruiz, 2017). Compounds consistent with isoprene-derived organochloride were recently observed in filter samples collected in Beijing (Le Breton et al., 2018).

Although all initial C_{8-12} alkane–Cl oxidation products are expected be nonchlorinated, formation of alkane-derived organochlorides is possible from Cl addition to multigenerational products. Studies show that the oxidation of alkanes with five or more linear carbons produces 1,4-hydroxycarbonyl that can undergo a rate-limiting, acid-catalyzed heterogeneous reaction to produce dihydrofuran (DHF) compounds (Atkinson et al., 2008; Holt et al., 2005; Jordan et al., 2008; Lim and Ziemann, 2009b, 2009c). DHF is highly reactive: for 2,5-dihydrofuran, the bimolecular reaction rate constants with O_3, OH and Cl are $1.65 \pm 0.31 \times 10^{-17}$, $6.45 \pm 1.69 \times 10^{-11}$, and $4.48 \pm 0.59 \times 10^{-10}$ cm^3 $molecule^{-1}$ s^{-1}, respectively (Alwe et al., 2013, 2014). Chlorine radicals can react with dihydrofuran via both H abstraction and Cl addition, producing chlorinated (e.g., dichlorotetrahydrofurans) and nonchlorinated compounds (e.g., furanones) under low NO_x conditions (Alwe et al., 2013). Similarly, formation of both chloronitrates (via Cl addition) and organonitrates (via H abstraction) from alkane–Cl oxidation is possible in the presence of NO_x. In this study, environmental chamber studies were conducted using long-chain (C_{8-12}) n-alkanes and Cl radicals under high-NO_x conditions to evaluate the Cl-initiated SOA formation from alkanes and to characterize the molecular composition of gas and aerosol compounds.

2 Methods

2.1 Environmental chamber experiments and instrumentation

Experiments were conducted inside a 10 m^3 Teflon® chamber at 298 K, using UV lights to generate radicals. The NO_2 photolysis rate was measured to characterize the UV intensity (Carter et al., 2005) and was found to be similar to ambient levels (0.53 min^{-1} at 0° zenith angle) at approximately 0.5 min^{-1}. The chamber relative humidity (RH) ranged from 0 to 67 %. For dry experiments, the chamber was filled with dried clean air supplied by a clean-air generator (model 737R, Aadco). Under typical atmospheric conditions, elevated RH can be expected, especially within the marine boundary layer near coastal regions, where Cl-alkane chemistry may be important (Riedel et al., 2012). Therefore, SOA formation under humid conditions was also investigated. For humid experiments (i.e., RH > 20 %), the chamber was flushed overnight with humidified clean air. To reduce wall loss, dried ammonium sulfate seed particles were injected into the chamber. The seed particles were generated from a 0.01 M aqueous ammonium sulfate solution using an aerosol generation system (AGS 2002, Brechtel). Chlorine gas (101 ppm in N_2, Airgas) was injected as the Cl radical precursor. Each n-alkane (n-octane at 99 %, n-decane

Table 1. Summary of experimental conditions and results.

Experiment no.	VOC	NO[a]	NO_2[a]	Cl_2[a]	RH	SOA	Y_{SOA}[b]	f_{44}[c]	f_{57}[d]	f_{HCl+}[e]	O_3[f]
1	Octane	35	2	40	5 >	19.5	0.28	1.1 E^{-1}	1.4 E^{-2}	1.1 to 1.3 E^{-2}	56
2	Octane	1	36	40	5 >	11.0	0.16	1.0 E^{-1}	1.6 E^{-2}	0.7 to 1.1 E^{-2}	69
3	Octane	17	19	40	5 >	16.6	0.24	1.5 E^{-1}	1.1 E^{-2}	0.8 to 1.0 E^{-2}	56
4	Octane	17	19	40	35	16.8	0.24	1.0 E^{-1}	1.3 E^{-2}	1.1 to 1.4 E^{-2}	60
5	Decane	32	0	40	5 >	68.3	0.84	1.0 E^{-1}	1.6 E^{-2}	0.7 to 1.1 E^{-2}	53
6	Decane	0	34	40	5 >	43.1	0.45	7.3 E^{-2}	1.7 E^{-2}	0.9 to 1.0 E^{-2}	61
7	Decane	19	18	40	5 >	64.7	0.80	1.3 E^{-1}	1.6 E^{-2}	0.9 to 1.2 E^{-2}	51
8	Decane	19	17	40	40	40.7	0.50	8.2 E^{-2}	1.7 E^{-2}	0.7 to 1.2 E^{-2}	57
9	Dodecane	35	1	40	5 >	148.6	1.65	2.1 E^{-1}	1.5 E^{-2}	0.6 to 0.8 E^{-2}	42
10	Dodecane	0	34	40	5 >	112.8	1.25	6.3 E^{-2}	2.5 E^{-2}	0.8 to 1.4 E^{-2}	54
11	Dodecane	17	18	40	5 >	126.4	1.40	6.8 E^{-2}	2.4 E^{-2}	0.9 to 1.4 E^{-2}	46
12	Dodecane	20	17	40	67	98.8	1.10	7.2 E^{-2}	2.5 E^{-2}	0.7 to 1.1 E^{-2}	62

NO, NO_2, O_3, and Cl_2 concentrations are in ppb. RH is in %. SOA concentration is in $\mu g\,m^{-3}$. Y_{SOA}, f_{44}, f_{57}, and f_{HCl+} are dimensionless. [a] Initial concentrations. [b] Y_{SOA} is calculated using the maximum SOA concentration and the initial precursor concentrations, which were 70 (octane), 81 (Decane), and 90 (dodecane) $\mu g\,m^{-3}$, assuming complete VOC consumption. [c] Mass ratio of organic ion fragments at m/z 44 (presumably mostly CO_2^+) to the sum of all organic ion fragments observed at peak SOA concentration. Used as a proxy for the SOA extent of oxidation. [d] Mass ratio of organic ion fragments at m/z 57 (presumably $C_4H_9^+$) to the sum of all organic ion fragments observed at peak SOA concentration. Used as a proxy for hydrocarbon-like organic aerosol. [e] Ratio of particulate chlorine mass (estimated using HCl^+ ion fragments in the ACSM) to organic mass. Lower value is the ratio observed at peak organic aerosol concentration and the higher value is the ratio observed at the peak particulate chlorine concentration. Particulate chlorine and organics peak at different times due to the rate-limiting heterogeneous production of dihydrofurans. Chloride concentrations were near-detection limits for octane experiments and may be more sensitive towards vaporizer interference effects (Wang and Hildebrandt Ruiz, 2017; Hu et al., 2017). [f] The amount of ozone observed when peak SOA concentration was observed.

at 99 %, dodecane > 99%; Sigma-Aldrich) was first injected into a glass gas sampling tube (Kimble-Chase, 250 mL), which was flushed with gently heated clean air into the chamber at 2 L min^{-1} for at least 30 min. Precursor NO (9.98 ppm in N_2, Airgas) and NO_2 (9.86 ppm in N_2, Airgas) were injected into the chamber using a mass flow controller (GFC17, Aalborg). Initial concentrations of VOC and oxidant precursors are summarized in Table 1. Gas-phase NO and NO_2 concentrations were monitored by a chemiluminescence monitor (200E, Teledyne). The O_3 concentration was monitored using a photometric ozone analyzer (400E, Teledyne). The start of photooxidation, initiated by turning on all the UV lights after the precursors were well mixed in the chamber, was designated as the reference point (i.e., time 0 min) for each experiment. UV lights were turned off after 60 min. The day before and after each SOA formation experiment, ammonium sulfate seed particles and 50 ppb of chlorine gas were injected into the chamber. UV lights were turned on to generate Cl radicals and remove residual reactive organic compounds in the chamber. Minimal SOA formation was observed during these cleaning experiments.

Particle size distributions were characterized using a scanning electrical mobility system (SEMS, Brechtel model 2002). The particle-phase bulk chemical composition was measured using an aerosol chemical speciation monitor (ACSM, Aerodyne). The ACSM was calibrated with 300 nm size-selected ammonium nitrate and ammonium sulfate aerosols generated from nebulized 0.005 M solutions using the AGS to determine the nitrate response factor (RF) and relative ionization efficiencies (RIE) for ammonium and sulfate, which are required for ion-to-mass signal conversions. Using electron impact ionization, the ACSM can measure the submicron, nonrefractory aerosol bulk composition at 1 min intervals (Budisulistiorini et al., 2013; Ng et al., 2011a). Using a standard fragmentation table (Allan et al., 2004), the ACSM can speciate the aerosol content into organics, nitrate, sulfate, ammonium, and chloride (Ng et al., 2011a). The ability of the ACSM to detect organic chloride using HCl^+ (m/z 36) has been demonstrated previously for isoprene–Cl SOA (Wang and Hildebrandt Ruiz, 2017). The default RIE_{Chl} value of 1.3 was used for chloride mass conversion. The Cl^+ (m/z 35) ion was excluded from chlorine quantification as it showed inconsistent response to nonrefractory chlorides (e.g., ammonium chloride). ACSM data were analyzed in Igor Pro V6.37 (Wavemetrics, Inc.) using ACSM local v1603 (Aerodyne) and other custom routines. Organic aerosol concentrations were calculated using ACSM measurements assuming a collection efficiency of 0.5 and RIE of 1.4, corrected for depositional particle wall loss (Pathak et al., 2007) but not for organic vapor loss (Huang et al., 2018b; Krechmer et al., 2017; Nah et al., 2017).

2.2 FIGAERO–CIMS

A high-resolution time-of-flight chemical ionization mass spectrometer (CIMS, Aerodyne) was used to measure the gas-phase chemical composition using I^- as the chemical ionization reagent. Humidified UHP N_2 was flushed over a methyl iodide permeation tube and then through ^{210}Po ionizer into the ion-molecule reaction chamber of the CIMS.

Theory and operation of the CIMS are described in detail elsewhere (Aljawhary et al., 2013; Bertram et al., 2011; Lee et al., 2014; Wang and Hildebrandt Ruiz, 2017). The CIMS inlet was coupled to a Filter Inlet for Gases and AEROsols (FIGAERO), which has been used in a number of studies to investigate the chemical composition and volatility of particle-phase compounds (D'Ambro et al., 2017; Gaston et al., 2016; Huang et al., 2018a; Lee et al., 2016; Lopez-Hilfiker et al., 2014, 2015; Stark et al., 2017; Thompson et al., 2017). The FIGAERO system alternated between two operational modes. In the aerosol collection mode, a gas-aerosol mixture was drawn through a PTFE filter (Zefluor® 2.0 µm 24 mm, Pall Corp.) at 3 SLPM for 15 to 45 min while gas species were sampled and analyzed. In the desorption mode, clean air or UHP N_2 was passed through the filter and heated to 200 °C (measured just above the filter) at a rate of approximately 5 to 10 °C min^{-1} for 40 to 20 min, respectively. The filter was then soaked at 200 °C for 20 min. The volatilized vapor was sampled by the CIMS, and the desorption signal as a function of temperature can be used to construct a one-dimensional (1-D) thermogram (e.g., Fig. 6a). For a monomeric compound, the desorption signal as a function of temperature is expected to be monomodal (Lopez-Hilfiker et al., 2014). The temperature at the peak desorption signal, T_{max} correlates with the enthalpy of sublimation (dH_{sub}) and the saturation vapor pressure (C^*) of the compound (Lopez-Hilfiker et al., 2014, 2015). However, some compounds may exhibit bimodal or multimodal behavior, with a second desorption mode occurring at much higher temperatures than expected, which is often interpreted as the result of thermal decomposition of larger oligomeric compounds (Huang et al., 2018a; Lopez-Hilfiker et al., 2014; Stark et al., 2017; Wang et al., 2016).

A FIGAERO–CIMS data analysis was conducted in Igor Pro with Tofware v2.5.10 (Tofwerk) and custom routines. Hundreds of ions belonging to diverse chemical families can be retrieved from the mass spectra. To simultaneously represent the chemical composition, relative aerosol volatility (i.e., T_{max} distribution), and multimodal thermal desorption behaviors, a two-dimensional (2-D) thermogram framework was developed. The 2-D thermogram is comprised of normalized unit-mass resolution 1-D thermograms, each expressed as a percentage color scale of the maximum desorption signal. Two-dimensional thermogram applications are discussed in Sect. 3.2. The advantage of using UMR over HR data is the ability to investigate the SOA thermal desorption behavior over the entire m/z and volatility (i.e., T_{max}) range without having to assign chemical formulae to all ion. This HR analysis is time consuming, especially for high-molecular-weight compounds, the exact molecular composition of which can be difficult to ascertain. The disadvantage of using UMR over HR data is the overlapping of ions and potential interference by isotopic signals or nonadduct ions. Therefore, the 2-D thermogram should be used as a complement rather than a replacement of the HR analysis. Based on the SOA molecular composition as observed by the FIGAERO–CIMS, the average oxidation state of carbon (OS_C) may be estimated:

$$OS_C = 2 \times O : C - H : C + NO_3 : C + Cl : C, \quad (1)$$

where $NO_3 : C$, $Cl : C$, $O : C$, and $H : C$ are the molecular ratios of the number of -NO_3 functional groups, -Cl functional groups, non-NO_3 oxygen atoms, and H atoms to the number of carbon atoms for any given compound. The average SOA OS_C is calculated based on iodide adducts only. For simplicity, all organic ions were assumed to have equal sensitivity, which is known to vary with ion cluster binding energy and sample RH (Hyttinen et al., 2018; Iyer et al., 2016; Lopez-Hilfiker et al., 2016).

3 Results and discussion

3.1 SOA and organic chloride formation

Experimental conditions and results are summarized in Table 1. Chlorine-alkane SOA yields increased with VOC precursor length, consistent with the trend observed for OH-alkane SOA (Jordan et al., 2008; Lim and Ziemann, 2009b; Presto et al., 2010; Schilling Fahnestock et al., 2015; Yee et al., 2012, 2013). For similarly functionalized alkane oxidation products, the vapor pressure decreases roughly loglinearly as the precursor carbon number increases from 8 to 15 (Jordan et al., 2008; Presto et al., 2010). Comparison of the unit-mass ACSM spectra for octane (Exp. 3), decane (Exp. 7), and dodecane (Exp. 11) SOA in Fig. S1 in the Supplement shows a consistent increase in the fractional contributions to the bulk OA mass (i.e., $f_{m/z}$) by organic ions at m/z 27 ($C_2H_3^+$), 41 ($C_3H_5^+$), 55 ($C_4H_7^+$) and 57 ($C_4H_9^+$) with increasing alkane length. Select odd m/z ions, noticeably m/z 55 and 57, have been used as tracers for hydrocarbon-like organic aerosol (HOA), and sometimes for primary aerosol emissions as well (Ng et al., 2011b; Ulbrich et al., 2009). Given the same oxidation conditions, SOA products derived from longer alkane precursors appeared less oxidized, as seen by the decrease in f_{44} (presumably mostly CO_2^+), but are more hydrocarbon-like, as seen by the increase in f_{57}, consistent with previous observations (Lambe et al., 2012; Loza et al., 2014). As the alkane chain length increases, the increased SOA production also favors the partitioning of semivolatile compounds into the particle phase (Donahue et al., 2006; Pankow, 1994), further lowering f_{44}.

Time series of gas-phase NO, NO_2, O_3, Cl_2, and suspended particle-phase organics and chlorine concentrations during photooxidation are shown in Fig. 1 using dodecane–Cl oxidation under low RH (Exp. 11) as the representative example. The Cl_2 concentration was estimated using I^- CIMS by tracking the Cl_2I^- ion. In addition, ions consistent with HO_2NO_2, HONO, and $ClNO_2$ were observed in the gas phase, as shown in Fig. 1. The $ClNO_2I^-$ ions are expected

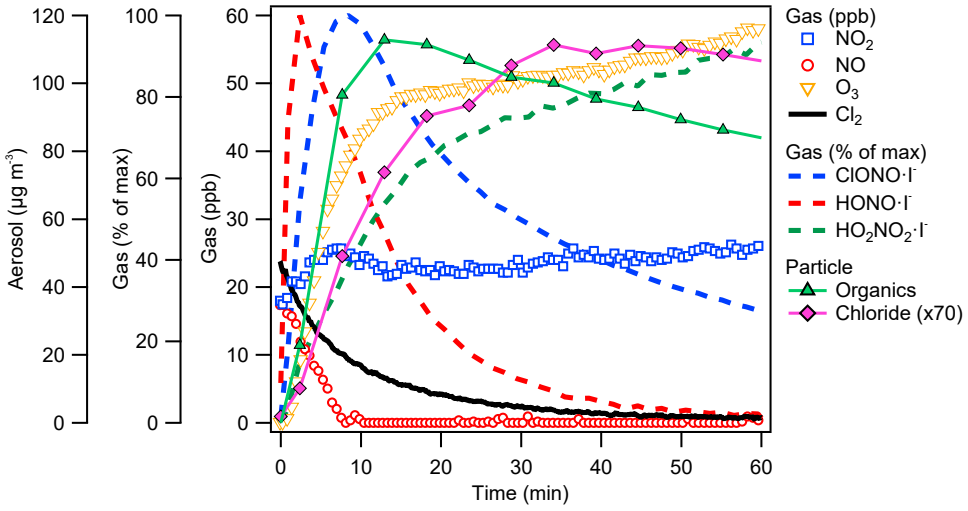

Figure 1. Representative trends of SOA and trace-gas species during the photooxidation period. Data from dodecane oxidation (Exp. 11) are shown. Particulate chlorine concentrations were multiplied by 70 for ease of comparison. Ions consistent with HONO and HO_2NO_2 were observed, indicative of secondary HO_x chemistry. Formation of ClONO and $ClNO_2$ due to oxidation of NO_2 by $Cl^•$ was also observed.

to correspond to both $ClNO_2$ (< 20 %) and chlorine nitrite (ClONO, > 80 %) from the reaction between $Cl^•$ and NO_2 (Golden, 2007; Niki et al., 1978). Formation of HO_2NO_2 from the reaction of HO_2 and NO_2 has been observed using I^- CIMS previously (Veres et al., 2015). Formation of HONO was likely due to the interactions between HO_x and NO (see Reactions S2 and S3 in the Supplement). Under UV, HONO decays to background levels. Production of HO_2NO_2 and HONO is indicative of secondary HO_x chemistry enabled by primary Cl-alkane oxidation chemistry, consistent with previous studies (Wang and Hildebrandt Ruiz, 2017; Young et al., 2014).

The NO concentration decreased sharply at the beginning of the photooxidation accompanied by increases in the concentrations of NO_2 and ozone. SOA production was most rapid during this initial period (0 to 10 min). Afterwards, at around 15 min in Fig. 1, the concentrations of NO_2 and ozone stabilized. Oxidation continued under UV driven by Cl radicals, and the SOA concentration began to decay due to oxidative fragmentation (Kroll et al., 2011; Lambe et al., 2012; Wang and Hildebrandt Ruiz, 2017) and wall loss. Ozone production continued slowly under UV at ~ 0.24 ppb min^{-1}. Slight NO_2 production (< 0.1 ppb min^{-1}) was also observed, which may be due to production of nitrous acid (HONO) on a Teflon® surface, a common background contaminant in environmental chambers (Carter et al., 2005; Rohrer et al., 2005).

SOA production was dependent on the initial NO and NO_2 concentrations, as shown in Fig. S2. Higher initial NO concentrations led to higher-SOA yields and lower ozone production for all precursors, as shown in Table 1 and Fig. S2. This is similar to alkane–OH SOA formation, where higher NO concentrations lead to more abundant organic nitrate formation, which increases the SOA volume (Schilling Fahnestock et al., 2015) and density (Loza et al., 2014). This is consistent with FIGAERO–CIMS results where the particulate organonitrate molar ratio (calculated as the average number of -NO_3 per molecule) and mass fraction were the highest in SOA produced under NO-only conditions (see Table S1 in Supplement). The organonitrate molar ratio also increased with the alkane precursor length, from 0.57–0.64 for octane to 0.75–0.93 for dodecane. A similar trend was observed for the organonitrate mass fraction, which increased from 0.53–0.58 for octane to 0.66–0.72 for dodecane. The alkane–Cl SOA yields, ranging from 0.16 (octane) to 1.65 (dodecane), are 4 times higher than the alkane–OH SOA yields (0.04 for octane and 0.35 for dodecane) that were obtained using 1 ppm alkane, 10 ppm methyl nitrite, and 10 ppm NO (Lim and Ziemann, 2009a), which are much higher than the precursor concentrations used here (13 to 15 ppb alkanes, < 40 ppb NO_x, 40 ppb Cl_2). Formation of primary alkyl nitrates due to terminal H abstraction by Cl could contribute to the higher SOA yields observed for alkane–Cl than for alkane–OH oxidation, as primary alkyl nitrates have lower saturation vapor pressures than secondary alkyl nitrates (Lim and Ziemann, 2009b; Yeh and Ziemann, 2014, 2015). The apparent SOA density, calculated using the ACSM SOA mass measurement and the SEMS SOA volume measurement, was 2.1 ± 0.3 g cm^{-3}, which is substantially higher than that reported for OH-alkane SOA formed under high-NO_x conditions, 1.06 to 1.28 g cm^{-3} (Lim and Ziemann, 2009a; Loza et al., 2014). These differences could be due to uncertainties associated with the ACSM and similar instruments, specifically the RIE (Li et al., 2018; Xu et al., 2018) and CE (Docherty et al., 2013; Middlebrook et al., 2012; Robinson et al., 2017), which may vary with SOA composition, oxidation state, or phase state. Assuming an

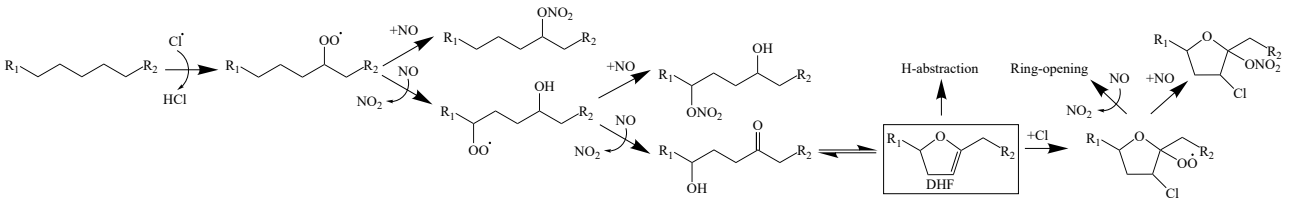

Figure 2. Formation pathway of chlorinated organics via chlorine addition to the DHF. H abstraction from DHF is also possible. Ozone may also react with the double-bond on the DHF, competing with chlorine radicals. Reaction pathways leading to DHF are adapted from OH-initiated oxidation of alkanes (Lim and Ziemann, 2009b).

SOA density of 1.06 g cm^{-3}, the SOA yield (0.10 to 0.99) is still higher for Cl-alkane oxidation compared to OH-alkane oxidation. Molar SOA yields, calculated using the average molecular weight of species identified with the FIGAERO–CIMS, are summarized in Table S1.

Although the initial Cl-alkane reactions proceed via a H-abstraction pathway, particulate chlorine was observed using the ACSM as shown in Fig. 1. Direct halogenation of the C_{8-12} alkyl radicals is expected to be minimal, given the low amounts of Cl_2 present (maximum of 40 ppb). A carbon–carbon double bond is required to enable Cl-addition reactions and organic chlorine formation. The heterogeneous production of dihydrofuran (DHF) via 1,4-hydroxycarbonyl uptake, acid-catalyzed isomerization, and dehydration reactions (Atkinson et al., 2008; Jordan et al., 2008; Lim and Ziemann, 2009c, b), followed by Cl addition to the DHF double bond, could be the source of observed organic chlorine. A condensed reaction pathway is shown in Fig. 2. The delay in particulate chlorine formation relative to that of bulk organics, as shown in Fig. 1, is consistent with the rate-limiting heterogeneous DHF production (Holt et al., 2005; Zhang et al., 2014). Under high-NO_x conditions, the peroxy radical product from the chlorine-addition pathway could react with NO to form a cyclic hemiacetal chloronitrate or an alkoxy radical that would undergo ring-opening reactions. Compounds resembling chloronitrates (e.g., $ONO_2{-}C_{12}H_{18}ClO_3 \cdot I^-$ for dodecane) were tentatively identified in the particle phase using the FIGAERO, but they were not well separated from the shoulder of nearby organonitrate peaks (e.g., $ONO_2{-}C_{12}H_{21}O_5 \cdot I^-$), as shown in Fig. S9. Select C_{2-6} organochlorides were well separated from nearby peaks and confirmed by the distinct Cl isotopic signal, the thermograms of which are shown in Fig. S10. The most abundant gas-phase organic chlorine compounds observed were products of ring-opening reaction pathways such as $C_2H_3ClO_2$ and C_{4-6} compounds. Small amounts of $C_2H_2Cl_2$ were also observed.

Organochloride formation is expected to be lower under humid conditions, where DHF formation is inhibited (Holt et al., 2005; Zhang et al., 2014; Ziemann, 2011). Evidence consistent with organochloride suppression under humid conditions was observed for dodecane SOA only, where the organochloride (including chloronitrates) mass fraction decreased from 0.15 (Exp. 11, <5 % RH) to 0.13 (Exp. 12, 67 % RH) as measured by the FIGAERO–CIMS. The mass fraction of the -Cl functional group decreased from 1.8 E^{-2} to 1.6 E^{-2} as measured by the FIGAERO–CIMS (Table S1) or from 1.4 E^{-2} to 1.1 E^{-2} as measured by the ACSM (Table 1) as the RH increased. No clear differences were observed for octane or decane SOA, which may be due to the less extreme RH conditions investigated, uncertainties with organochloride ion identification in the CIMS, or the lower organochloride concentrations observed in Exps. 1–8, which is especially challenging for chloride quantification using the ACSM.

DHF ozonolysis can compete with chlorination. For instance, under typical marine boundary layer (MBL) conditions, the chlorine-initiated oxidation was estimated to be a significant sink of 2,5-DHF, accounting for 29 % of the reaction in the presence of OH and O_3 (Alwe et al., 2014). In contrast, only 1.8 % of 2,3-DHF consumption was attributed to Cl radical chemistry in the MBL, owing to the increased reactivity of 2,3-DHF (relative to 2,5-DHF) towards ozone and OH radicals (Alwe et al., 2014). The reported alkane–OH reaction mechanisms expect the formation of substituted 2,3-DHF (Ziemann, 2011). The alkane-derived organochloride yield under ambient conditions is therefore expected to be smaller in the presence of elevated RH and O_3 levels. Although ozone can impose an upper limit on alkane SOA yields and oxidation state, suppressing the multigenerational OH-alkane oxidation chemistry (Zhang et al., 2014), the continued gas-phase processing of OH-alkane and DHF-ozonolysis products via H abstraction by chlorine radicals could counteract these limitations.

The gas-phase alkane–Cl oxidation products formed under high-NO_x conditions were dominated by organonitrates, which was also reflected in the dominance of organonitrates in the particles phase (see Table 1 and Sect. 3.2). Figure 3 shows the formation of early-generation (e.g., hydroxynitrates, $ONO_2{-}C_nH_{2n+1}O$) and multigenerational (e.g., oxidized organonitrates, $ONO_2{-}C_nH_{2n-5}O_4$) oxidation products from different alkane precursors. Like the bulk particle-phase composition, gas-phase compounds derived from smaller alkane precursor were more oxidized given similar oxidation conditions (e.g., NO, NO_2, and Cl_2): the signal of oxidation products with similar oxygen numbers

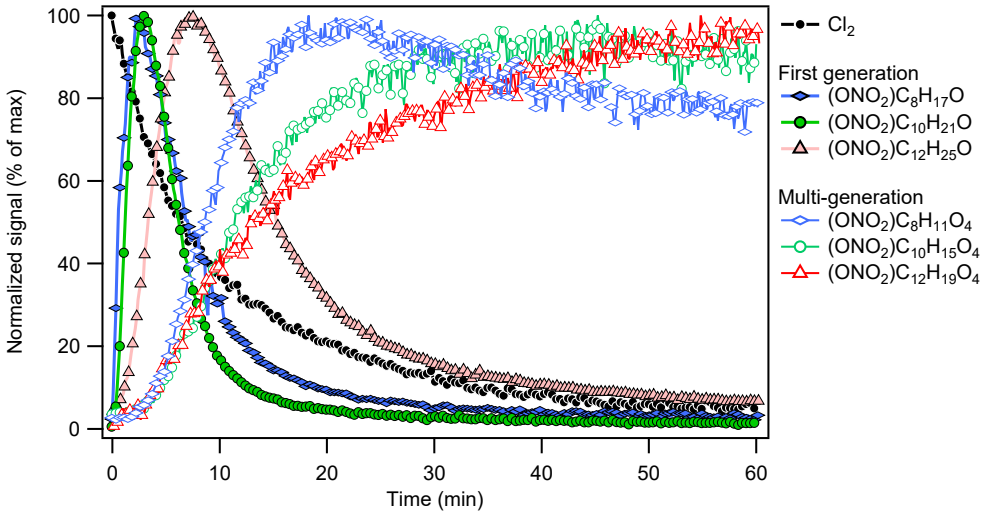

Figure 3. Trends of early-generation gas-phase oxidation products (hydroxynitrates) and multigeneration-oxidation products (hydroxycarbonyl nitrates) observed during chlorine-initiated oxidation of octane (Exp. 3), decane (Exp. 7), and dodecane (Exp. 11). Species shown were first normalized against the I^- reagent ion signal and then normalized against their respective maxima.

(and higher oxidation state) peaked earlier in the photooxidation period for smaller precursors (e.g., $ONO_2{-}C_8H_{11}O_4$ vs. $ONO_2{-}C_{12}H_{19}O_4$ in Fig. 3). As oxidation continued, driven primarily by gas-phase chemistry (Aimanant and Ziemann, 2013), the importance of fragmentation reactions increased relative to that of functionalization reactions (Lambe et al., 2012). The heterogeneous oxidation of SOA (Bertram et al., 2001; George and Abbatt, 2010), which is expected to drive the oxidation of very large ($n > 30$) alkanes (Lim and Ziemann, 2009b), may also contribute to oxidation and fragmentation observed here, but its impacts are beyond the scope of this work. Assuming a uniform CIMS sensitivity, Figure 4a shows that the gas phase was dominated by C_3 to C_5 organic nitrates. Figure 4b shows that the OS_C increased, while n_C decreased as photooxidation continued, indicative of fragmentation reactions. In addition to hydroxynitrates and hydroxycarbonyl nitrates, dinitrates and trinitrates were also observed. The CIMS was not sensitive towards simple, alkane-derived alkyl nitrates ($ONO_2{-}C_nH_{2n+1}$). The lack of sensitivity of the I^- reagent ion towards simple alkyl and keto nitrates has been reported previously for isoprene- and monoterpene-derived organic nitrates (Lee et al., 2016).

3.2 Two-dimensional thermogram

The FIGAERO filter spectra are shown in Fig. 4c for octane (Exp. 3), decane (Exp. 7), and dodecane (Exp. 11). A logscale version of Fig. 4c is shown in Fig. S3. The spectra are calculated from the average desorption ion signals observed when the filter temperature was between 40 and 140 °C. As shown below and in Fig. 5, SOA components desorbed most effectively in this temperature range, with most organic ions having T_{max} within this temperature range. At desorption temperature above 140 °C, inorganic ions began to dominate the spectra. The C_{8-12} alkane–Cl SOA share many similarities towards the lower m/z (< 320) range, which consisted of $C_{\leq 7}$ oxidized organic compounds. For larger alkane precursors, the particle-phase composition was dominated by C_n organic nitrates, which are grouped by their degree of oxygenation (i.e., number of nonnitrate O atoms), O_x, as shown in Fig. 4c. O_1 to O_5 mononitrates, O_2 to O_4 dinitrates, and O_1 to O_3 trinitrates dominated each oxygenation group. O_6 to O_8 mononitrates were present in the particle phase but were less abundant than the nearby O_2 to O_4 dinitrates (e.g., $(ONO_2)_2{-}C_{12}H_{20}O_2$ at m/z 447 > $(ONO_2)_2{-}C_{12}H_{22}O_2$ at m/z 449 > $(ONO_2){-}C_{12}H_{17}O_6$ m/z 446 > $(ONO_2){-}C_{12}H_{19}O_6$ at m/z 448). An example of a C_{12} mononitrate distribution is shown in Fig. S4. Assuming the same sensitivity towards the different organic nitrates observed, the organic nitrate abundance follows a bell-shaped distribution, similarly to field observations for C_5 and C_{10} organic nitrates derived from isoprene and monoterpenes, respectively (Lee et al., 2016). For dodecane mononitrates, the abundance peaked around O_3 and O_4 and decreased towards O_2 and O_5, as shown in Fig. S4. Dinitrate abundance decreased from O_2 to O_4. Trinitrate decreased from O_1 to O_3. Similar trends can be observed for octane and decane SOA. As the precursor length increased, the SOA appeared less oxidized, as shown in Fig. 4d, consistent with ACSM observations for f_{44} (see Table 1 and Fig. S1), which is correlated with OS_C (Canagaratna et al., 2015). Simple hydroxynitrates (e.g., $ONO_2{-}C_nH_{2n+1}O$) were not observed in the particle phase as they were completely oxidized in the gas phase, as shown in Fig. 3.

In addition to the identification of aerosol chemical composition, the FIGAERO–CIMS can be used to estimate the

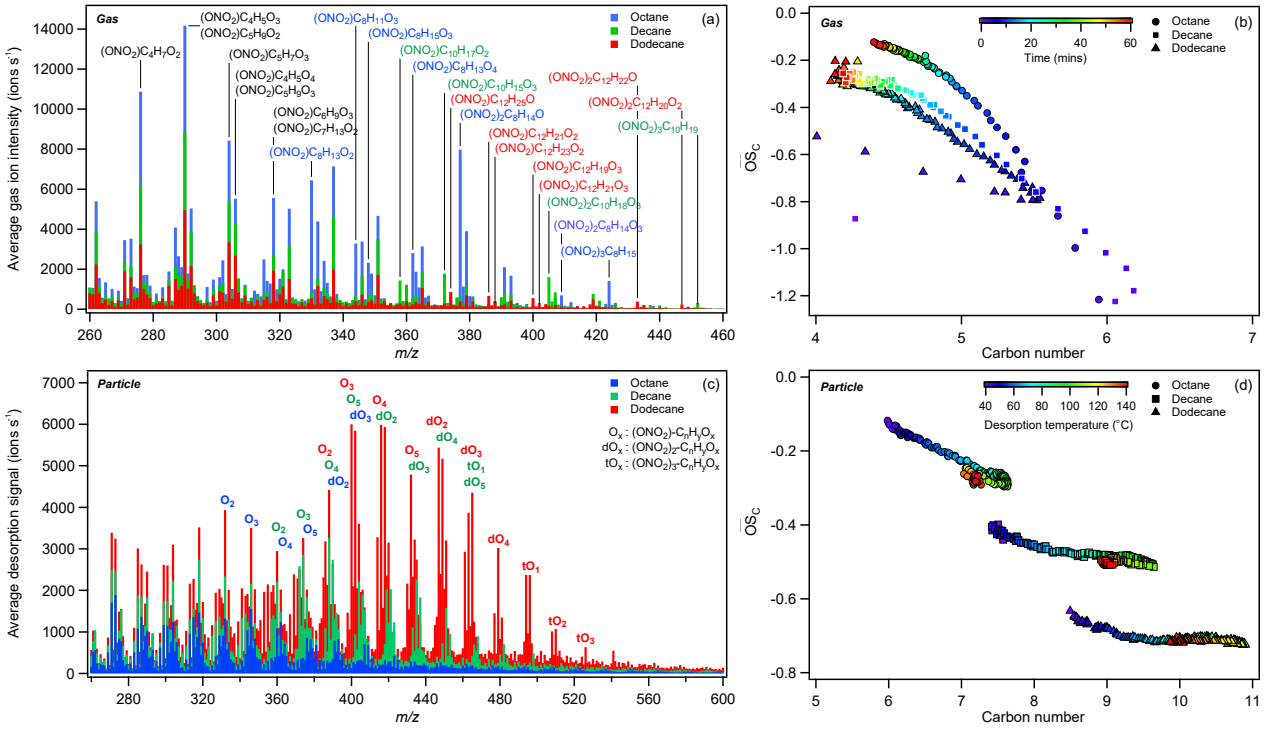

Figure 4. Comparison of the **(a)** average composition and **(b)** the increases in average OS_C of gas-phase reaction products over the photooxidation period (0–60 min), as well as the **(c)** average particle-phase composition and **(d)** the evolution of average SOA OS_C during FIGAERO desorption for octane (Exp. 3), decane (Exp. 7), and dodecane (Exp. 11). Color-coded ions in **(a)** and **(c)** indicate molecules that were much more abundant in reaction products derived from a particular alkane precursor. In **(c)**, O_x, dO_x, and tO_x were used as shorthand notations for oxidized organic nitrate, dinitrate, and trinitrates with x number of oxygens (excluding those from ONO_2). Sticks in **(a)** and **(c)** were not stacked, and no x-axis offset was applied during plotting. In **(b)**, OS_C increased and n_C decreased as photooxidation continued, consistent with photooxidative fragmentation. In **(d)**, SOA derived from larger alkane precursors appeared less oxidized, consistent with results shown in Table 1 and Fig. S1. Methods used to calculate the average OS_C and n_C are detailed in the Supplement.

aerosol volatility using empirical correlations between C* and T_{max} (Lopez-Hilfiker et al., 2014, 2015). The particle-phase chemical composition and volatility distribution can be represented in several ways. For instance, desorption signals of select compounds can be normalized against the maximum and plotted on the same 1-D thermogram (ion signal vs. filter temperature) to compare their relative volatilities (Lopez-Hilfiker et al., 2014). Scatterplots of oxygen number or O : C ratio vs. carbon number colored by T_{max} or particle-phase mass fraction have been used to show changes in aerosol composition (Huang et al., 2018a; Lopez-Hilfiker et al., 2014, 2015). To show the differences between various types of thermal desorption products (i.e., monomers, thermal decomposition products, and oligomers), averages of the 1-D thermograms can be shown (Huang et al., 2018a; Lopez-Hilfiker et al., 2015). Scatterplots of T_{max} or the OS_c vs. molecular weight have been used to distinguish monomers and oligomers for select compounds (Wang et al., 2016). Here we propose a new framework to represent aerosol composition, relative volatility, and oligomer decomposition simultaneously using 2-D thermograms shown in Fig. 5a–e.

As illustrated in Fig. 5a for octane–chlorine SOA, the thermal desorption products can be separated into five different groups. Region 1 ($m/z < 350$, $40 < T_{max} < 90\,^{\circ}C$) was composed of a group of semivolatile compounds with similar T_{max} values. Iodide adducts in this region correspond to species that are too volatile to be present as molecular compounds in the particle phase and are likely low-temperature decomposition products. A prominence of ions smaller than m/z 127 including Cl^- and a range of organic ions could be due to acid exchange or charge transfer products (as opposed to I^- adducts) of low-temperature decomposition products. Although I^- is a relatively soft ionization method compared to electron impact ionization, collision-induced ion fragmentation and cluster dissociation cannot be ruled out as a potential source for nonadducts. Region 2 ($350 < m/z < \sim 700$, $40\,^{\circ}C < T_{max} < 120\,^{\circ}C$) consisted of monomers, dimers, and some oligomers. Oligomerization may proceed via condensed-phase reactions between cyclic hemiacetal compounds, forming acetal dimers, or reactions between cyclic hemiacetal and 1,4-hydroxycarbonyl compounds, forming hemiacetal dimers (Aimanant and Ziemann,

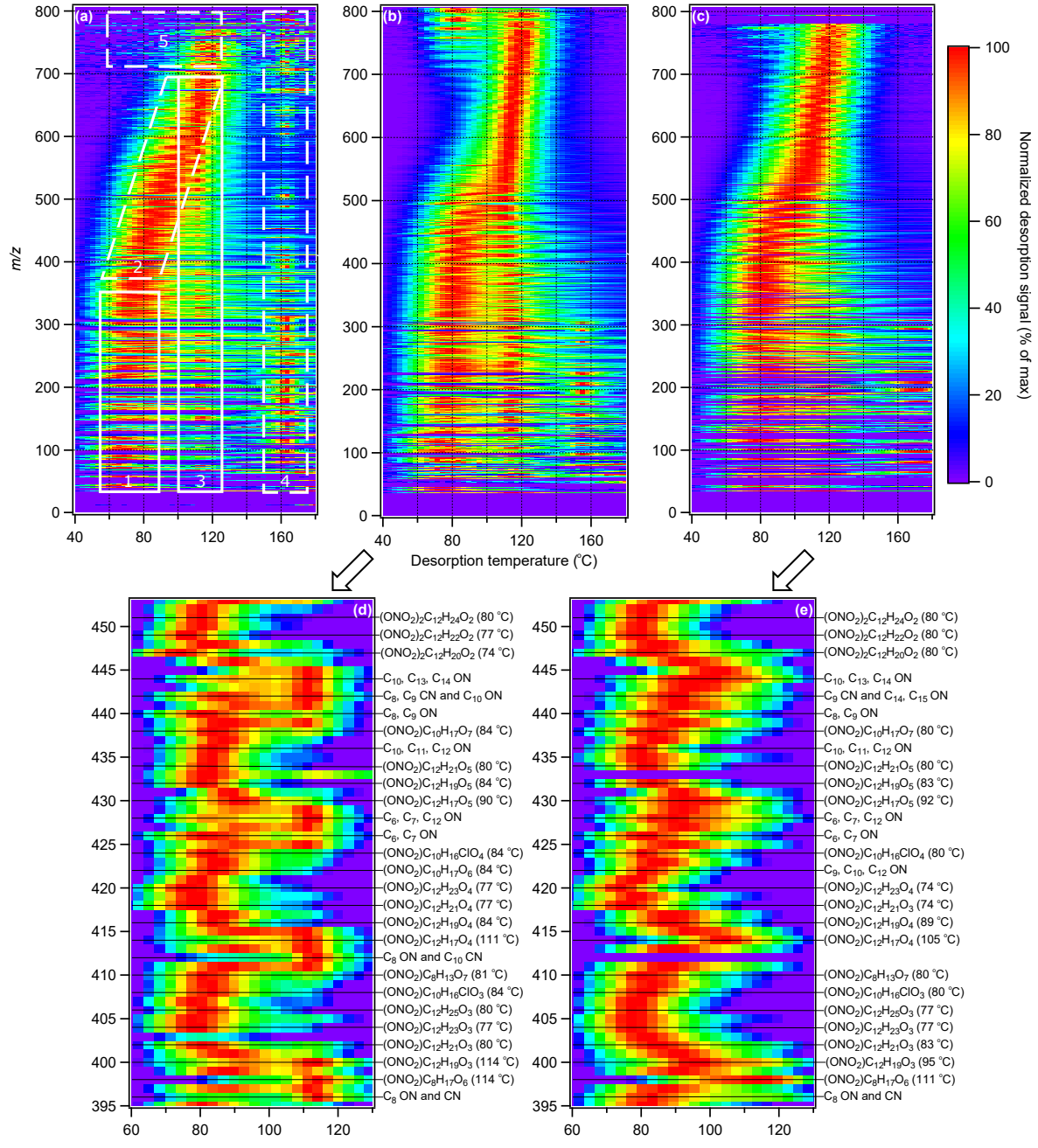

Figure 5. Comparison of two-dimensional thermograms for **(a)** octane–Cl SOA under low RH from Exp. 3, **(b)** dodecane–Cl SOA under low RH from Exp. 11, and **(c)** dodecane–Cl SOA under high RH (67 %) from Exp. 12. The color represents the ion intensity at a m/z as a percentage of the maximum desorption signal observed at that m/z. Different thermal desorption regions in **(a)** are dominated by (1) low-temperature thermal decomposition products and nonadducts (2) monomers (3) oligomers and their decomposition products and (4) thermal decomposition of ammonium sulfate or extremely low-volatility compounds. Region (5) is unresolved but appears to be thermally unstable oligomers. Region (2) and (3) can overlap, as shown in **(d)** for **(b)** and as shown in **(e)** for **(c)**. At each nominal m/z, only the dominant ion is labeled in **(d)** and **(e)**. If multiple ions of similar intensity were present, only general descriptions are given in the annotations, where ON stands for organonitrate and CN stands for chloronitrate. Nonnitrated organic ions were observed but not labeled because they were positioned between more intense organonitrates at neighboring m/z coordinates. T_{max} values are included in parenthesis. Increasing the RH suppressed oligomer formation, enhancing the monomer features in **(c)** and **(e)** when compared with **(b)** and **(d)**. The m/z values shown includes the chemical ionization reagent I^- (m/z 127).

2013). Condensed-phase, acid-catalyzed isomerization of hemiacetal and acetal dimers is also possible (Aimanant and Ziemann, 2013). For OH-initiated oxidation of dodecane under high-NO_x conditions, hemiacetals and nitrate hemiacetals are reported to dominate the oligomer composition (Schilling Fahnestock et al., 2015), where nitrate hemiacetals could form via the reactive uptake of hydroxy dihydrofuran and hydroxycarbonyl nitrate compounds (Schilling Fahnestock et al., 2015). The three oligomerization pathways are illustrated in Fig. S11. Ions consistent with acetal, hemiacetal, and nitrate hemiacetal compounds were observed in the particle phase using the FIGAERO–CIMS in regions 2 and 3. Oligomer formation via aldol condensation by highly oxidized compounds is also possible (Schilling Fahnestock et al., 2015). Oligomerization may also proceed through a NO_3 elimination and a reverse esterification process involving two alkyl nitrate compounds to form a single nitrate oligomer, which was recently proposed for α-Pinene SOA, though the exact mechanism remains elusive (Faxon et al., 2018).

An overall positive correlation between T_{max} and molecular weight was observed in region 2. A similar correlation was also reported for SOA derived from oleic acid (Wang et al., 2016) and from α-Pinene (Faxon et al., 2018). In other words, overall, volatility decreased with molecular weight for compounds in region 2. However, within small m/z segments in region 2, the correlation was not strictly linear and the T_{max} varied cyclically. When the carbon and oxygen numbers were fixed (i.e., fixed O : C), the T_{max} decreased (i.e., volatility increased) with increasing H : C (i.e., decreasing OS_C), as shown in Fig. 5e for C_{12} organic nitrates (e.g., $ONO_2{-}C_{12}H_{19-25}O_3 \cdot I^-$ from m/z 400 to 406) observed in dodecane–Cl SOA desorption. Although decreases in OS_C are often associated with increases in the aerosol volatility (Donahue et al., 2011; Kroll et al., 2011), fragmentation notwithstanding, the increase in H : C in each fixed O : C ion group was expected to decrease in aerosol volatility. The increase in H : C was likely due to increased hydroxy functionalization over ketone functionalization, which should result in lowering of the saturation vapor pressure according to group contribution theory (Pankow and Asher, 2008). In addition, the T_{max} decreased from $O_3 : C_{12}$ organonitrates (e.g., $ONO_2{-}C_{12}H_{21}O_3$, T_{max} 95 °C) to $O_4 : C_{12}$ organonitrates (e.g., $ONO_2{-}C_{12}H_{21}O_4$, T_{max} 89 °C). The inconsistencies observed within small m/z segments may be due to loading-dependent T_{max} shift (see Sect. 3.3), where T_{max} increases with mass loading. As shown in Fig. 4c, the organonitrate ion intensities decreased from O_3 onwards. Overlapping of monomer and oligomer desorption peaks could also increase the apparent T_{max}.

Region 3 ($T_{max} > 90$ °C) consisted of thermal decomposition products across a wide m/z range. Select ions were present in both region 2 and region 3, resulting in bimodal thermal desorption, which can complicate T_{max} estimation using the 2-D thermogram, especially when ions from the two desorption modes overlap. The thermal decomposition products may be the result of reversible dissociation of oligomers (Faxon et al., 2018; Schobesberger et al., 2018) or the cleavage of C-O or C-C bonds, which has been observed in the thermal decomposition of monomeric organic acids (Stark et al., 2017). Additionally, SOA may exist in a "glassy" state (Koop et al., 2011), trapping volatile components (Perraud et al., 2012) that are released as the SOA mass is depleted. Region 4 (150 °C < T_{max} < 170 °C) consisted of mostly thermal decomposition products of the $(NH_4)_2SO_4$ seed particles. There was a clear gap between region 3 and 4. It is possible that the edge of regions 2 and 3, towards a high T_{max} range, is the FIGAERO–CIMS's volatility detection limit for alkane–Cl SOA, where the energy required for vaporization exceeds that for thermal decomposition (Lopez-Hilfiker et al., 2014). Plateauing of T_{max} towards the high m/z range of region 2 appeared to agree with this hypothesis, for which further increases in molecular weight, carbon number, and the degree of oxidation translated to negligible T_{max} increase. Region 5 ($m/z > 700$) likely consisted of high molecular weight, low volatility oligomers. Region 5 therefore likely consisted of C_{24-36+} (dimers and above) compounds. Thermal desorption of some high-molecular-weight compounds at temperatures much lower than expected ($T_{max} \sim 80$ °C) was observed for decane SOA and dodecane SOA. No definitive molecular composition was determined for these ions due to low signal intensity and wide range of potential chemical formulae.

The region boundaries can vary depending on the SOA composition as well as mass loading, as will be discussed in Sect. 3.3. The distribution and general features of the regions are consistent for alkane–Cl SOA formed in different experiments (Figs. 5 and S8). Comparison of 2-D thermograms for octane–Cl SOA (Fig. 5a) and dodecane–Cl SOA (Fig. 5b) shows that the dodecane SOA contains unique, high-molecular-weight oligomers ($m/z > 750$), which are accompanied by significantly stronger thermal decomposition features in region 3. Bimodal thermal desorption behavior was observed, as shown in Fig. 5d, which masked the volatility m/z dependence expected for region 2. Compared to SOA formed under dry conditions (Fig. 5b, Exp. 11), SOA formed under humid conditions (Exp. 12, 67 % RH) contained less high-molecular-weight oligomers in region 5 and exhibited much less thermal decomposition behavior in region 3, as shown in Fig. 5e, where a more distinct T_{max}-m/z correlation could be established compared to Fig. 5d. RH-induced oligomer suppression has been reported for toluene and α-Pinene SOA formation (Hinks et al., 2018; Huang et al., 2018a). The oligomer decrease under high RH could also be due to RH-volatility dependent organic vapor wall loss (Huang et al., 2018b). A clear m/z dependence of signal reduction under humid conditions compared to the dry conditions is shown in Fig. S5. Additionally, SOA yield decreased (37 % for decane and 22 % for dodecane) under humid conditions while ozone production increased, which could be related to humidity-induced inhibition of 1,4-hydroxycarbonyl

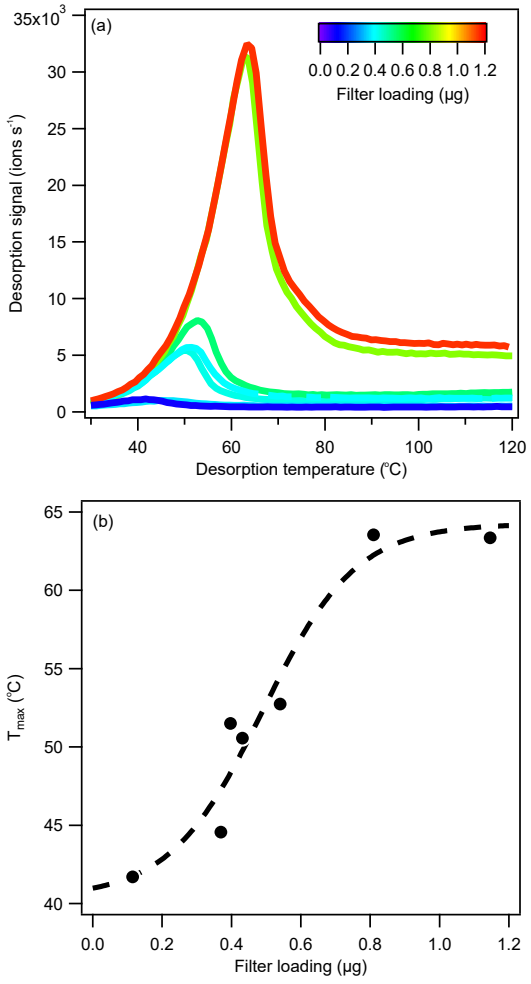

Figure 6. **(a)** The 1-D thermograms for levoglucosan ($C_6H_{10}O_5$) at different loading conditions and **(b)** the correlation between filter loading and T_{max}. Levoglucosan aerosol was generated by nebulizing a 1.2 E^{-2} M aqueous solution. The aerosol was injected into the clean Teflon chamber, collected onto the FIGAERO filter, and analyzed. The T_{max}-loading correlation for pure levoglucosan could be described by a sigmoid function, leveling off at 41 and 64 °C under very low and very high loading conditions, respectively.

uptake and heterogeneous DHF formation (Holt et al., 2005). DHF is a key intermediate product for multigenerational oxidation chemistry and is reactive towards ozone (Zhang et al., 2014; Ziemann, 2011). Reduction in SOA yields under humid conditions has also been reported for dodecane–OH SOA formation (Schilling Fahnestock et al., 2015). The combined effects of DHF reduction and ozone enhancement would suppress organic chloride formation, which was observed for dodecane SOA, as discussed in Sect. 3.1.

3.3 T_{max} shift

As the desorption temperature increased above 140 °C, all dominant ions observed shared the same T_{max}, except for some background ions (e.g., $IHNO_3^-$), as shown in Fig. 5a–c, which were identified to be related to the thermal decomposition of $(NH_4)_2SO_4$ seed particles. From this process, H_2SO_4 vapor molecules produced were either detected as $H_2SO_4 \cdot I^-$ or were deprotonated to produce HSO_4^-, acting as a secondary chemical ionization reagent. Examples of first-order (e.g., HSO_4^-), second-order (e.g., $H_2SO_4 \cdot HSO_4^-$) and third-order sulfate (e.g., $(H_2SO_4)_2 \cdot HSO_4^-$) clusters are shown in Fig. S6. It is worth noting that, while the T_{max} of sulfate ions was uniform within each filter desorption run, the T_{max} varied between filter runs, which can be seen in Fig. 5a–c to be between 146 and 153 °C. Characterization experiments suggested that T_{max} may increase with filter loading, as shown in Fig. 6a for pure levoglucosan aerosols and in Fig. S7a for pure $(NH_4)_2SO_4$ aerosols. Whereas the T_{max}-mass loading correlation appeared to be linear for pure $(NH_4)_2SO_4$, as shown in Fig. S7b. for T_{max} between 136 and 149 °C, a roughly sigmoidal correlation was observed for pure levoglucosan, as shown in Fig. 6b, where T_{max} increased quickly from 43 to 62 °C as filter loading increased from 0.2 to 0.8 µg.

T_{max} shift phenomena have been observed in several FIGAERO–CIMS studies (D'Ambro et al., 2017; Gaston et al., 2016; Huang et al., 2018a; Lopez-Hilfiker et al., 2015; Thompson et al., 2017). Explanations vary for the observed T_{max} shifts. For example, pinonic acid ($C_{10}H_{16}O_3$) identified in α-Pinene ozonolysis SOA had a much higher T_{max} (40 °C) than expected from calibration (T_{max} < 32 °C), which was attributed to interactions between pinonic acid and other SOA components, causing a decrease in the measured apparent vapor pressure (Lopez-Hilfiker et al., 2015). However, no matrix effects were reported for the pinonic acid T_{max} value (now around 65 °C instead of < 32 °C) obtained from a synthetic mixture of organic acid calibrants (Thompson et al., 2017), where some interactions between different organic molecules might have been expected. Whereas the pure compounds are shown to have sharp monomodal desorption peaks (Lopez-Hilfiker et al., 2014), the field campaign-average thermograms for individual compounds have broader desorption peaks (Thompson et al., 2017), which could be due to the presence of isomers (Thompson et al., 2017), variations in filter loading, differences in aerosol viscosity (Huang et al., 2018a), or interferences from oligomer decomposition products (Lopez-Hilfiker et al., 2014). Another T_{max} shift example was reported for ambient biomass burning measurements, where the levoglucosan T_{max} varied between 58–70 °C, in the range of the 61.5 °C literature value (Lopez-Hilfiker et al., 2014) and the values observed here (41–64 °C), between 17:00 and 10:00 over the course of the campaign (Gaston et al., 2016). Between 10:00 and 19:00, the levoglucosan T_{max} was significantly higher at 100 °C, which was attributed to thermal decomposition of oligomers produced from acid-catalyzed heterogenous reactions, as indicated by the increase in sulfate ion intensities during the same period (Gaston et al.,

2016). It was not clear whether the sulfate ions measured were derived from sulfuric acid or from the decomposition of $(NH_4)_2SO_4$, which could change the assumption made for aerosol acidity. A T_{max} shift was also observed for isoprene SOA, where the mass and T_{max} of nonnitrated OA decreased with increasing NO_x concentration (D'Ambro et al., 2017). A recent investigation reported increases in T_{max} for α-Pinene ozonolysis SOA produced under dry conditions compared to SOA produced under humid conditions (Huang et al., 2018a). A positive correlation between aerosol loading and T_{max} was reported for the first time, and the uniform thermal desorption peak shape assumption was questioned (Huang et al., 2018a). The loading dependence was reported to plateau at around 2 to 4 µg (converted from CIMS ion intensity assuming maximum sensitivity, i.e., that of formic acid), similarly to observations for levoglucosan standards as shown in Fig. 6b, possibly due to saturation effects. Because increased oligomer content was observed under dry conditions, the authors suggested that viscosity effects were responsible for the observed T_{max} shift (Huang et al., 2018a). It should be noted that plateauing of the T_{max}-loading dependence was demonstrated using averaged values, where ions were lumped based on carbon number. Those that had less than or equal to 10 carbons were designated as monomers, which likely included desorption ions across multiple desorption regions (see Fig. 5). This categorization was perhaps too broad, and the loading dependence of individual ions could be lost after averaging. In contrast, the T_{max} of oligomers, which were defined as compounds that contained more than 10 carbons – thus were a more precisely defined group – only began to plateau at higher concentrations.

The T_{max} mass dependence was also observed for alkane–Cl SOA. For Exp. 6, three filters were collected and analyzed. The first filter was collected at 3 SLPM for 45 min, followed by the second filter at 3 SLPM for 30 min, and afterwards the third filter at 3 SLPM for 15 min. The ratios of the unit-mass integrated ion signals during the desorption period for the first two filters relative to that of the third filter are shown in Fig. S8a. The associated 2-D thermograms are shown in Fig. S8b–d. Compounds in the T_{max}-m/z dependence region (Region 2) showed a 10 to 20 °C T_{max} increase from the lowest filter-loading to the highest filter-loading conditions. T_{max} of sulfate-related ions increased from 149 to 172 °C with filter loading. The increase of enhancement ratio with m/z, as shown in Fig. S8a, reflects the changes in the composition of suspended aerosol in the chamber over time. Between the first (high-loading) filter collection and the third (low-loading) filter collection, volatility-dependent vapor wall loss may lead to a disproportionate decrease in high-molecular-weight, low-volatility compounds (Huang et al., 2018b; Krechmer et al., 2016), resulting in increasingly greater enhancement towards the high m/z region shown in Fig. S8a. The correlation between T_{max} shift and integrated desorption signal for organics was not linear, unlike for ammonium sulfate, which may be due to matrix or saturation effects as previously suggested (Huang et al., 2018a). T_{max}-loading dependence may differ for individual FIGAEROs due to design variations or artifacts such as sample distribution within the filter matrix or nonuniform heating, which would result in different aerosol evaporation kinetics (Schobesberger et al., 2018). Overall, our results show that the T_{max} for organic and inorganic compounds varies with loading, which needs to be accounted for when estimating aerosol component volatility from the empirical correlations between T_{max} and C^* using the FIGAERO–CIMS.

4 Conclusions

Environmental chamber experiments were carried out to investigate the chlorine-initiated oxidation of C_{8-12} linear alkanes under high-NO_x conditions. Rapid SOA formation and ozone production were observed. SOA yields increase with precursor length, consistent with alkane–OH SOA formation. Under similar oxidation conditions, alkane–Cl SOA exhibited more hydrocarbon-like characteristics as the alkane precursor length increased, as indicated by the ACSM measurements. This bulk SOA observation is consistent with gas- and particle-phase CIMS measurements, which identified more oxidized reaction products derived from smaller alkane precursors. CIMS measurements also suggest that organonitrates dominated the gas- and particle-phase composition. Trace amounts of alkane-derived organochlorides were observed using the ACSM and the FIGAERO–CIMS, likely produced via chlorine addition to the heterogeneously produced dihydrofuran compounds. Organochloride and bulk SOA production were suppressed under humid conditions, whereas ozone production increased. Under such conditions, the SOA yields observed for chlorine-initiated oxidation of octane (0.24), decane (0.50), and dodecane (1.10) were still much higher than those observed for OH-initiated oxidation of the respective alkanes. Overall, these results show that chlorine-alkane oxidation could be an important pathway for SOA production and aging, especially in highly polluted environments replete with alkane, NO_x, and reactive chlorine emission sources.

A clear mass-loading dependence for T_{max} from FIGAERO–CIMS data was demonstrated using levoglucosan, ammonium sulfate, and alkane–Cl SOA, indicating that the quantitative assessment of C^* from T_{max} using the FIGAERO–CIMS needs to account for variations in filter loading. A unit-mass-resolution 2-D FIGAERO–CIMS thermogram framework was developed. The 2-D thermograms demonstrate a clear relationship between molecular weight and volatility of aerosol components, and RH-induced suppression of oligomer formation. When used in conjunction with high-resolution ion fitting, the 2-D thermogram can be a powerful tool for interpreting the chemical composition and volatility distribution of particle-phase compounds.

Data availability. Data published in this paper's figures and tables are available via the Texas Data Repository, https://doi.org/10.18738/T8/4PFPSO (Wang and Hildebrandt Ruiz, 2018). Underlying research data are also available by request to Lea Hildebrandt Ruiz: lhr@che.utexas.edu.

The Supplement related to this article is available online at: https://doi.org/10.5194/acp-18-15535-2018-supplement

Author contributions. DSW performed the experiments, data analysis, and manuscript preparation, overseen by LHR. Both authors contributed to the experimental design and interpretation of results.

Competing interests. The authors declare that they have no conflict of interest.

Acknowledgements. This material is based on work supported by the Welch Foundation under grant no. F-1925 and the National Science Foundation under grant no. 1653625. We thank Paul J. Ziemann and Lucas B. Algrim for helpful discussions on the formation of organochlorides. We thank the Air & Waste Management Association for the Air Quality Research and Study Scholarship.

Edited by: Manabu Shiraiwa
Reviewed by: two anonymous referees

References

Ahern, A. T., Goldberger, L., Jahl, L., Thornton, J., and Sullivan, R. C.: Production of N_2O_5 and $ClNO_2$ through Nocturnal Processing of Biomass-Burning Aerosol, Environ. Sci. Technol., 52, 550–559, https://doi.org/10.1021/acs.est.7b04386, 2018.

Aimanant, S. and Ziemann, P. J.: Chemical mechanisms of aging of aerosol formed from the reaction of n-pentadecane with OH radicals in the presence of NO_x, Aerosol Sci. Technol., 47, 979–990, https://doi.org/10.1080/02786826.2013.804621, 2013.

Aljawhary, D., Lee, A. K. Y., and Abbatt, J. P. D.: High-resolution chemical ionization mass spectrometry (ToF-CIMS): Application to study SOA composition and processing, Atmos. Meas. Tech., 6, 3211–3224, https://doi.org/10.5194/amt-6-3211-2013, 2013.

Allan, J. D., Delia, A. E., Coe, H., Bower, K. N., Alfarra, M. R., Jimenez, J. L., Middlebrook, A. M., Drewnick, F., Onasch, T. B., Canagaratna, M. R., Jayne, J. T., and Worsnop, D. R.: A generalised method for the extraction of chemically resolved mass spectra from Aerodyne aerosol mass spectrometer data, J. Aerosol Sci., 35, 909–922, https://doi.org/10.1016/j.jaerosci.2004.02.007, 2004.

Alwe, H. D., Walawalkar, M., Sharma, A., Pushpa, K. K., Dhanya, S., and Naik, P. D.: Rate coefficients for the gas-phase reactions of chlorine atoms with cyclic ethers at 298 K, Int. J. Chem. Kinet., 45, 295–305, https://doi.org/10.1002/kin.20765, 2013.

Alwe, H. D., Walavalkar, M. P., Sharma, A., Dhanya, S., and Naik, P. D.: Tropospheric oxidation of cyclic unsaturated ethers in the day-time: Comparison of the reactions with Cl, OH and O_3 based on the determination of their rate coefficients at 298 K, Atmos. Environ., 82, 113–120, https://doi.org/10.1016/j.atmosenv.2013.10.009, 2014.

Aschmann, S. M. and Atkinson, R.: Rate constants for the gas-phase reactions of alkanes with Cl atoms at 296 ± 2 K, Int. J. Chem. Kinet., 27, 613–622, https://doi.org/10.1002/kin.550270611, 1995.

Atkinson, R. and Arey, J.: Atmospheric Degradation of Volatile Organic Compounds, Chem. Rev., 103, 4605–4638, https://doi.org/10.1021/cr0206420, 2003.

Atkinson, R., Arey, J., and Aschmann, S. M.: Atmospheric chemistry of alkanes: Review and recent developments, Atmos. Environ., 42, 5859–5871, https://doi.org/10.1016/j.atmosenv.2007.08.040, 2008.

Bahreini, R., Middlebrook, A. M., Brock, C. A., de Gouw, J. A., McKeen, S. A., Williams, L. R., Daumit, K. E., Lambe, A. T., Massoli, P., Canagaratna, M. R., Ahmadov, R., Carrasquillo, A. J., Cross, E. S., Ervens, B., Holloway, J. S., Hunter, J. F., Onasch, T. B., Pollack, I. B., Roberts, J. M., Ryerson, T. B., Warneke, C., Davidovits, P., Worsnop, D. R., and Kroll, J. H.: Mass Spectral Analysis of Organic Aerosol Formed Downwind of the Deepwater Horizon Oil Spill: Field Studies and Laboratory Confirmations, Environ. Sci. Technol., 46, 8025–8034, https://doi.org/10.1021/es301691k, 2012.

Bertram, A. K., Ivanov, A. V., Hunter, M., Molina, L. T., and Molina, M. J.: The reaction probability of OH on organic surfaces of tropospheric interest, J. Phys. Chem. A, 105, 9415–9421, https://doi.org/10.1021/jp0114034, 2001.

Bertram, T. H., Kimmel, J. R., Crisp, T. A., Ryder, O. S., Yatavelli, R. L. N., Thornton, J. A., Cubison, M. J., Gonin, M., and Worsnop, D. R.: A field-deployable, chemical ionization time-of-flight mass spectrometer, Atmos. Meas. Tech., 4, 1471–1479, https://doi.org/10.5194/amt-4-1471-2011, 2011.

Budisulistiorini, S. H., Canagaratna, M. R., Croteau, P. L., Marth, W. J., Baumann, K., Edgerton, E. S., Shaw, S. L., Knipping, E. M., Worsnop, D. R., Jayne, J. T., Gold, A., and Surratt, J. D.: Real-time continuous characterization of secondary organic aerosol derived from isoprene epoxydiols in downtown Atlanta, Georgia, using the aerodyne aerosol chemical speciation monitor, Environ. Sci. Technol., 47, 5686–5694, https://doi.org/10.1021/es400023n, 2013.

Cai, X. and Griffin, R. J.: Secondary aerosol formation from the oxidation of biogenic hydrocarbons by chlorine atoms, J. Geophys. Res.-Atmos., 111, 1–14, https://doi.org/10.1029/2005JD006857, 2006.

Cai, X., Ziemba, L. D., and Griffin, R. J.: Secondary aerosol formation from the oxidation of toluene by chlorine atoms, Atmos. Environ., 42, 7348–7359, https://doi.org/10.1016/j.atmosenv.2008.07.014, 2008.

Canagaratna, M. R., Jimenez, J. L., Kroll, J. H., Chen, Q., Kessler, S. H., Massoli, P., Hildebrandt Ruiz, L., Fortner, E., Williams, L. R., Wilson, K. R., Surratt, J. D., Donahue, N. M., Jayne, J. T., and Worsnop, D. R.: Elemental ratio measurements of organic compounds using aerosol mass spectrometry: Characterization, improved calibration, and implications, Atmos. Chem. Phys., 15, 253–272, https://doi.org/10.5194/acp-15-253-2015, 2015.

Caravaggio, G. A., Charland, J. P., Macdonald, P., and Graham, L.: N-Alkane Profiles of Engine Lubricating Oil and Particulate Matter By Molecular Sieve Extraction, Environ. Sci. Technol., 41, 3697–3701, https://doi.org/10.1021/es062233h, 2007.

Carlton, A. G., Bhave, P. V, Napelenok, S. L., Edney, E. D., Sarwar, G., Pinder, R. W., Pouliot, G. A., and Houyoux, M.: Model Representation of Secondary Organic Aerosol in CMAQv4.7, Environ. Sci. Technol., 44, 8553–8560, https://doi.org/10.1021/es100636q, 2010.

Carter, W. P. L., Cocker, D. R., Fitz, D. R., Malkina, I. L., Bumiller, K., Sauer, C. G., Pisano, J. T., Bufalino, C., and Song, C.: A new environmental chamber for evaluation of gas-phase chemical mechanisms and secondary aerosol formation, Atmos. Environ., 39, 7768–7788, https://doi.org/10.1016/j.atmosenv.2005.08.040, 2005.

Chang, S., Tanaka, P., Mcdonald-buller, E., and Allen, D. T.: Emission inventory for atomic chlorine precursors in Southeast Texas, Rep. Contract 9880077600-18 between Univ. Texas Texas Nat. Resour. Conserv. Comm., 1–27, 2001.

Chrit, M., Sartelet, K., Sciare, J., Pey, J., Marchand, N., Couvidat, F., Sellegri, K., and Beekmann, M.: Modelling organic aerosol concentrations and properties during ChArMEx summer campaigns of 2012 and 2013 in the western Mediterranean region, Atmos. Chem. Phys., 17, 12509–12531, https://doi.org/10.5194/acp-17-12509-2017, 2017.

D'Ambro, E. L., Lee, B. H., Liu, J., Shilling, J. E., Gaston, C. J., Lopez-Hilfiker, F. D., Schobesberger, S., Zaveri, R. A., Mohr, C., Lutz, A., Zhang, Z., Gold, A., Surratt, J. D., Rivera-Rios, J. C., Keutsch, F. N., and Thornton, J. A.: Molecular composition and volatility of isoprene photochemical oxidation secondary organic aerosol under low- and high-NO_x conditions, Atmos. Chem. Phys., 17, 159–174, https://doi.org/10.5194/acp-17-159-2017, 2017.

DeCarlo, P. F., Ulbrich, I. M., Crounse, J., De Foy, B., Dunlea, E. J., Aiken, A. C., Knapp, D., Weinheimer, A. J., Campos, T., Wennberg, P. O., and Jimenez, J. L.: Investigation of the sources and processing of organic aerosol over the Central Mexican Plateau from aircraft measurements during MILAGRO, Atmos. Chem. Phys., 10, 5257–5280, https://doi.org/10.5194/acp-10-5257-2010, 2010.

de Gouw, J. A., Middlebrook, A. M., Warneke, C., Ahmadov, R., Atlas, E. L., Bahreini, R., Blake, D. R., Brock, C. A., Brioude, J., Fahey, D. W., Fehsenfeld, F. C., Holloway, J. S., Le Henaff, M., Lueb, R. A., McKeen, S. A., Meagher, J. F., Murphy, D. M., Paris, C., Parrish, D. D., Perring, A. E., Pollack, I. B., Ravishankara, A. R., Robinson, A. L., Ryerson, T. B., Schwarz, J. P., Spackman, J. R., Srinivasan, A., and Watts, L. A.: Organic Aerosol Formation Downwind from the Deepwater Horizon Oil Spill, Science, 331, 1295–1299, https://doi.org/10.1126/science.1200320, 2011.

Docherty, K. S., Jaoui, M., Corse, E., Jimenez, J. L., Offenberg, J. H., Lewandowski, M., and Kleindienst, T. E.: Collection Efficiency of the Aerosol Mass Spectrometer for Chamber-Generated Secondary Organic Aerosols, Aerosol Sci. Technol., 47, 294–309, https://doi.org/10.1080/02786826.2012.752572, 2013.

Donahue, N. M., Robinson, A. L., Stanier, C. O., and Pandis, S. N.: Coupled partitioning, dilution, and chemical aging of semivolatile organics, Environ. Sci. Technol., 40, 2635–2643, https://doi.org/10.1021/es052297c, 2006.

Donahue, N. M., Epstein, S. A., Pandis, S. N., and Robinson, A. L.: A two-dimensional volatility basis set: 1. organic-aerosol mixing thermodynamics, Atmos. Chem. Phys., 11, 3303–3318, https://doi.org/10.5194/acp-11-3303-2011, 2011.

Dunmore, R. E., Hopkins, J. R., Lidster, R. T., Lee, J. D., Evans, M. J., Rickard, A. R., Lewis, A. C., and Hamilton, J. F.: Diesel-related hydrocarbons can dominate gas phase reactive carbon in megacities, Atmos. Chem. Phys., 15, 9983–9996, https://doi.org/10.5194/acp-15-9983-2015, 2015.

Dzepina, K., Volkamer, R. M., Madronich, S., Tulet, P., Ulbrich, I. M., Zhang, Q., Cappa, C. D., Ziemann, P. J., and Jimenez, J. L.: Evaluation of recently-proposed secondary organic aerosol models for a case study in Mexico City, Atmos. Chem. Phys., 9, 5681–5709, https://doi.org/10.5194/acp-9-5681-2009, 2009.

Faxon, C., Hammes, J., Le Breton, M., Pathak, R. K., and Hallquist, M.: Characterization of organic nitrate constituents of secondary organic aerosol (SOA) from nitrate-radical-initiated oxidation of limonene using high-resolution chemical ionization mass spectrometry, Atmos. Chem. Phys., 18, 5467–5481, https://doi.org/10.5194/acp-18-5467-2018, 2018.

Faxon, C. B. and Allen, D. T.: Chlorine chemistry in urban atmospheres: A review, Environ. Chem., 10, 221–233, https://doi.org/10.1071/EN13026, 2013.

Finlayson-Pitts, B. J.: Halogens in the troposphere, Anal. Chem., 82, 770–776, https://doi.org/10.1021/ac901478p, 2010.

Fraser, M. P., Cass, G. R., Simoneit, B. R. T., and Rasmussen, R. A.: Air quality model evaluation data for organics, 4. C_2–C_{36} nonaromatic hydrocarbons, Environ. Sci. Technol., 31, 2356–2367, https://doi.org/10.1021/es960980g, 1997.

Gaston, C. J., Lopez-Hilfiker, F. D., Whybrew, L. E., Hadley, O., McNair, F., Gao, H., Jaffe, D. A., and Thornton, J. A.: Online molecular characterization of fine particulate matter in Port Angeles, WA: Evidence for a major impact from residential wood smoke, Atmos. Environ., 138, 99–107, https://doi.org/10.1016/j.atmosenv.2016.05.013, 2016.

George, I. J. and Abbatt, J. P. D.: Heterogeneous oxidation of atmospheric aerosol particles by gas-phase radicals, Nat. Chem., 2, 713–722, https://doi.org/10.1038/nchem.806, 2010.

Golden, D. M.: The Reaction $Cl + NO_2 \rightarrow ClONO$ and $ClNO_2$, J. Phys. Chem. A, 111, 6772–6780, https://doi.org/10.1021/jp069000x, 2007.

Goldstein, A. H. and Galbally, I. E.: Known and unexplored organic constituents in the earth's atmosphere, Environ. Sci. Technol., 41, 1514–1521, https://doi.org/10.1021/es072476p, 2007.

Guenther, A. B., Jiang, X., Heald, C. L., Sakulyanontvittaya, T., Duhl, T., Emmons, L. K., and Wang, X.: The model of emissions of gases and aerosols from nature version 2.1 (MEGAN2.1): An extended and updated framework for modeling biogenic emissions, Geosci. Model Dev., 5, 1471–1492, https://doi.org/10.5194/gmd-5-1471-2012, 2012.

Hinks, M. L., Montoya-Aguilera, J., Ellison, L., Lin, P., Laskin, A., Laskin, J., Shiraiwa, M., Dabdub, D., and Nizkorodov, S. A.: Effect of relative humidity on the composition of secondary organic aerosol from the oxidation of toluene, Atmos. Chem. Phys., 18, 1643–1652, https://doi.org/10.5194/acp-18-1643-2018, 2018.

Holt, T., Atkinson, R., and Arey, J.: Effect of water vapor concentration on the conversion of a series of 1,4-hydroxycarbonyls

to dihydrofurans, J. Photoch. Photobio. A, 176, 231–237, https://doi.org/10.1016/j.jphotochem.2005.08.029, 2005.

Hoyle, C. R., Boy, M., Donahue, N. M., Fry, J. L., Glasius, M., Guenther, A., Hallar, A. G., Huff Hartz, K., Petters, M. D., Petäjä, T., Rosenoern, T., and Sullivan, A. P.: A review of the anthropogenic influence on biogenic secondary organic aerosol, Atmos. Chem. Phys., 11 321–343, https://doi.org/10.5194/acp-11-321-2011, 2011.

Hu, W., Campuzano-Jost, P., Day, D. A., Croteau, P., Canagaratna, M. R., Jayne, J. T., Worsnop, D. R., and Jimenez, J. L.: Evaluation of the new capture vaporizer for aerosol mass spectrometers (AMS) through field studies of inorganic species, Aerosol Sci. Technol., 51, 735–754, https://doi.org/10.1080/02786826.2017.1296104, 2017.

Huang, M., Liu, X., Hu, C., Guo, X., Gu, X., Zhao, W., Wang, Z., Fang, L., and Zhang, W.: Aerosol laser time-of-flight mass spectrometer for the on-line measurement of secondary organic aerosol in smog chamber, Meas. J. Int. Meas. Confed., 55, 394–401, https://doi.org/10.1016/j.measurement.2014.05.038, 2014.

Huang, W., Saathoff, H., Pajunoja, A., Shen, X., Naumann, K.-H., Wagner, R., Virtanen, A., Leisner, T., and Mohr, C.: α-Pinene secondary organic aerosol at low temperature: chemical composition and implications for particle viscosity, Atmos. Chem. Phys., 18, 2883–2898, https://doi.org/10.5194/acp-18-2883-2018, 2018a.

Huang, Y., Zhao, R., Charan, S. M., Kenseth, C. M., Zhang, X., and Seinfeld, J. H.: Unified Theory of Vapor-Wall Mass Transport in Teflon-Walled Environmental Chambers, Environ. Sci. Technol., 52, 2134–2142, https://doi.org/10.1021/acs.est.7b05575, 2018b.

Hyttinen, N., Otkjær, R. V., Iyer, S., Kjaergaard, H. G., Rissanen, M. P., Wennberg, P. O., and Kurtén, T.: Computational Comparison of Different Reagent Ions in the Chemical Ionization of Oxidized Multifunctional Compounds, J. Phys. Chem. A, 122, 269–279, https://doi.org/10.1021/acs.jpca.7b10015, 2018.

Iyer, S., Lopez-Hilfiker, F., Lee, B. H., Thornton, J. A., and Kurtén, T.: Modeling the Detection of Organic and Inorganic Compounds Using Iodide-Based Chemical Ionization, J. Phys. Chem. A, 120, 576–587, https://doi.org/10.1021/acs.jpca.5b09837, 2016.

Jordan, C. E., Ziemann, P. J., Griffin, R. J., Lim, Y. B., Atkinson, R., and Arey, J.: Modeling SOA formation from OH reactions with C_8–C_{17} n-alkanes, Atmos. Environ., 42, 8015–8026, https://doi.org/10.1016/j.atmosenv.2008.06.017, 2008.

Karlsson, R. S., Szente, J. J., Ball, J. C., and Maricq, M. M.: Homogeneous aerosol formation by the chlorine atom initiated oxidation of toluene, J. Phys. Chem. A, 105, 82–96, https://doi.org/10.1021/jp001831u, 2001.

Khare, P. and Gentner, D. R.: Considering the future of anthropogenic gas-phase organic compound emissions and the increasing influence of non-combustion sources on urban air quality, Atmos. Chem. Phys., 18, 5391–5413, https://doi.org/10.5194/acp-18-5391-2018, 2018.

Kleeman, M. J., Riddle, S. G., Robert, M. A., and Jakober, C. a.: Lubricating oil and fuel contributions to particulate matter emissions from light-duty gasoline and heavy-duty diesel vehicles, Environ. Sci. Technol., 42, 235–42, https://doi.org/10.1021/es071054c, 2008.

Koop, T., Bookhold, J., Shiraiwa, M., and Pöschl, U.: Glass transition and phase state of organic compounds: Dependency on molecular properties and implications for secondary organic aerosols in the atmosphere, Phys. Chem. Chem. Phys., 13, 19238–19255, https://doi.org/10.1039/c1cp22617g, 2011.

Krechmer, J. E., Pagonis, D., Ziemann, P. J., and Jimenez, J. L. L.: Quantification of gas-wall partitioning in Teflon environmental chambers using rapid bursts of low-volatility oxidized species generated in-situ, Environ. Sci. Technol., 50, 5757–5765, https://doi.org/10.1021/acs.est.6b00606, 2016.

Krechmer, J. E., Day, D. A., Ziemann, P. J., and Jimenez, J. L.: Direct Measurements of Gas/Particle Partitioning and Mass Accommodation Coefficients in Environmental Chambers, Environ. Sci. Technol., 51, 11867–11875, https://doi.org/10.1021/acs.est.7b02144, 2017.

Kroll, J. H., Donahue, N. M., Jimenez, J. L., Kessler, S. H., Canagaratna, M. R., Wilson, K. R., Altieri, K. E., Mazzoleni, L. R., Wozniak, A. S., Bluhm, H., Mysak, E. R., Smith, J. D., Kolb, C. E., and Worsnop, D. R.: Carbon oxidation state as a metric for describing the chemistry of atmospheric organic aerosol, Nat. Chem., 3, 133–139, https://doi.org/10.1038/nchem.948, 2011.

Kwok, E. S. C. and Atkinson, R.: Estimation of hydroxyl radical reaction rate constants for gas phase organic compounds using a structure-reactivity relationship: An update, Atmos. Environ., 29, 1685–1695, https://doi.org/10.1016/1352-2310(95)00069-B, 1995.

Lambe, A. T., Onasch, T. B., Croasdale, D. R., Wright, J. P., Martin, A. T., Franklin, J. P., Massoli, P., Kroll, J. H., Canagaratna, M. R., Brune, W. H., Worsnop, D. R., and Davidovits, P.: Transitions from functionalization to fragmentation reactions of laboratory Secondary Organic Aerosol (SOA) generated from the OH oxidation of alkane precursors, Environ. Sci. Technol., 46, 5430–5437, https://doi.org/10.1021/es300274t, 2012.

Lamkaddam, H., Gratien, A., Pangui, E., Cazaunau, M., Picquet-Varrault, B., and Doussin, J. F.: High-NOx Photooxidation of n-Dodecane: Temperature Dependence of SOA Formation, Environ. Sci. Technol., 51, 192–201, https://doi.org/10.1021/acs.est.6b03821, 2017.

Le Breton, M., Hallquist, Å. M., Pathak, R. K., Simpson, D., Wang, Y., Johansson, J., Zheng, J., Yang, Y., Shang, D., Wang, H., Liu, Q., Chan, C., Wang, T., Bannan, T. J., Priestley, M., Percival, C. J., Shallcross, D. E., Lu, K., Guo, S., Hu, M., and Hallquist, M.: Chlorine oxidation of VOCs at a semi-rural site in Beijing: significant chlorine liberation from $ClNO_2$ and subsequent gas- and particle-phase Cl–VOC production, Atmos. Chem. Phys., 18, 13013–13030, https://doi.org/10.5194/acp-18-13013-2018, 2018.

Lee, B. H., Lopez-Hilfiker, F. D., Mohr, C., Kurtén, T., Worsnop, D. R., and Thornton, J. A.: An iodide-adduct high-resolution time-of-flight chemical-ionization mass spectrometer: Application to atmospheric inorganic and organic compounds, Environ. Sci. Technol., 48, 6309–6317, https://doi.org/10.1021/es500362a, 2014.

Lee, B. H., Mohr, C., Lopez-Hilfiker, F. D., Lutz, A., Hallquist, M., Lee, L., Romer, P., Cohen, R. C., Iyer, S., Kurtén, T., Hu, W., Day, D. A., Campuzano-Jost, P., Jimenez, J. L., Xu, L., Ng, N. L., Guo, H., Weber, R. J., Wild, R. J., Brown, S. S., Koss, A., de Gouw, J., Olson, K., Goldstein, A. H., Seco, R., Kim, S., McAvey, K., Shepson, P. B., Starn, T., Baumann, K., Edgerton, E. S., Liu, J., Shilling, J. E., Miller, D. O., Brune, W., Schobesberger, S., D'Ambro, E. L., and Thornton, J. A.: Highly functionalized organic nitrates in the southeast United

States: Contribution to secondary organic aerosol and reactive nitrogen budgets, P. Natl. Acad. Sci. USA, 113, 201508108, https://doi.org/10.1073/pnas.1508108113, 2016.

Li, X., Ma, Y., Chen, H., Jiang, Y., Ma, X., Yin, R., Yang, D., Shi, X., Hao, J., Jiang, J., and Zheng, J.: Sensitivity of a Q-ACSM to chamber generated SOA with different oxidation states, Atmos. Meas. Tech. Discuss., https://doi.org/10.5194/amt-2018-45, in review, 2018.

Lim, Y. B. and Ziemann, P. J.: Products and mechanism of secondary organic aerosol formation from reactions of n-alkanes with OH radicals in the presence of NO_x, Environ. Sci. Technol., 39, 9229–9236, https://doi.org/10.1021/es051447g, 2005.

Lim, Y. B. and Ziemann, P. J.: Effects of molecular structure on aerosol yields from OH radical-initiated reactions of linear, branched, and cyclic alkanes in the presence of NO_x, Environ. Sci. Technol., 43, 2328–2334, https://doi.org/10.1021/es803389s, 2009a.

Lim, Y. B. and Ziemann, P. J.: Chemistry of Secondary Organic Aerosol Formation from OH Radical-Initiated Reactions of Linear, Branched, and Cyclic Alkanes in the Presence of NO_x, Aerosol Sci. Technol., 43, 604–619, https://doi.org/10.1080/02786820902802567, 2009b.

Lim, Y. B. and Ziemann, P. J.: Kinetics of the heterogeneous conversion of 1,4-hydroxycarbonyls to cyclic hemiacetals and dihydrofurans on organic aerosol particles, Phys. Chem. Chem. Phys., 11, 8029, https://doi.org/10.1039/b904333k, 2009c.

Lopez-Hilfiker, F. D., Mohr, C., Ehn, M., Rubach, F., Kleist, E., Wildt, J., Mentel, T. F., Lutz, A., Hallquist, M., Worsnop, D., and Thornton, J. A.: A novel method for online analysis of gas and particle composition: Description and evaluation of a filter inlet for gases and AEROsols (FIGAERO), Atmos. Meas. Tech., 7, 983–1001, https://doi.org/10.5194/amt-7-983-2014, 2014.

Lopez-Hilfiker, F. D., Mohr, C., Ehn, M., Rubach, F., Kleist, E., Wildt, J., Mentel, T. F., Carrasquillo, a. J., Daumit, K. E., Hunter, J. F., Kroll, J. H., Worsnop, D. R., and Thornton, J. A.: Phase partitioning and volatility of secondary organic aerosol components formed from α-pinene ozonolysis and OH oxidation: the importance of accretion products and other low volatility compounds, Atmos. Chem. Phys., 15, 7765–7776, https://doi.org/10.5194/acp-15-7765-2015, 2015.

Lopez-Hilfiker, F. D., Iyer, S., Mohr, C., Lee, B. H., D'ambro, E. L., Kurtén, T., and Thornton, J. A.: Constraining the sensitivity of iodide adduct chemical ionization mass spectrometry to multifunctional organic molecules using the collision limit and thermodynamic stability of iodide ion adducts, Atmos. Meas. Tech., 9, 1505–1512, https://doi.org/10.5194/amt-9-1505-2016, 2016.

Loza, C. L., Craven, J. S., Yee, L. D., Coggon, M. M., Schwantes, R. H., Shiraiwa, M., Zhang, X., Schilling, K. A., Ng, N. L., Canagaratna, M. R., Ziemann, P. J., Flagan, R. C., and Seinfeld, J. H.: Secondary organic aerosol yields of 12-carbon alkanes, Atmos. Chem. Phys., 14, 1423–1439, https://doi.org/10.5194/acp-14-1423-2014, 2014.

Lyon, D. R., Zavala-Araiza, D., Alvarez, R. A., Harriss, R., Palacios, V., Lan, X., Talbot, R., Lavoie, T., Shepson, P., Yacovitch, T. I., Herndon, S. C., Marchese, A. J., Zimmerle, D., Robinson, A. L., and Hamburg, S. P.: Constructing a Spatially Resolved Methane Emission Inventory for the Barnett Shale Region, Environ. Sci. Technol., 49, 8147–8157, https://doi.org/10.1021/es506359c, 2015.

McDonald, B. C., De Gouw, J. A., Gilman, J. B., Jathar, S. H., Akherati, A., Cappa, C. D., Jimenez, J. L., Lee-Taylor, J., Hayes, P. L., McKeen, S. A., Cui, Y. Y., Kim, S. W., Gentner, D. R., Isaacman-VanWertz, G., Goldstein, A. H., Harley, R. A., Frost, G. J., Roberts, J. M., Ryerson, T. B., and Trainer, M.: Volatile chemical products emerging as largest petrochemical source of urban organic emissions, Science, 359, 760–764, https://doi.org/10.1126/science.aaq0524, 2018.

Middlebrook, A. M., Bahreini, R., Jimenez, J. L., and Canagaratna, M. R.: Evaluation of Composition-Dependent Collection Efficiencies for the Aerodyne Aerosol Mass Spectrometer using Field Data, Aerosol Sci. Technol., 46, 258–271, https://doi.org/10.1080/02786826.2011.620041, 2012.

Minguillón, M. C., Perron, N., Querol, X., Szidat, S., Fahrni, S. M., Alastuey, A., Jimenez, J. L., Mohr, C., Ortega, A. M., Day, D. A., Lanz, V. A., Wacker, L., Reche, C., Cusack, M., Amato, F., Kiss, G., Hoffer, A., Decesari, S., Moretti, F., Hillamo, R., Teinilä, K., Seco, R., Peñuelas, J., Metzger, A., Schallhart, S., Müller, M., Hansel, A., Burkhart, J. F., Baltensperger, U., and Prévót, A. S. H.: Fossil versus contemporary sources of fine elemental and organic carbonaceous particulate matter during the DAURE campaign in Northeast Spain, Atmos. Chem. Phys., 11, 12067–12084, https://doi.org/10.5194/acp-11-12067-2011, 2011.

Minguillón, M. C., Pérez, N., Marchand, N., Bertrand, A., Temime-Roussel, B., Agrios, K., Szidat, S., van Drooge, B., Sylvestre, A., Alastuey, A., Reche, C., Ripoll, A., Marco, E., Grimalt, J. O., and Querol, X.: Secondary organic aerosol origin in an urban environment: influence of biogenic and fuel combustion precursors, Faraday Discuss., 189, 337–359, https://doi.org/10.1039/C5FD00182J, 2016.

Murphy, B. N. and Pandis, S. N.: Simulating the Formation of Semivolatile Primary and Secondary Organic Aerosol in a Regional Chemical Transport Model, Environ. Sci. Technol., 43, 4722–4728, https://doi.org/10.1021/es803168a, 2009.

Nah, T., McVay, R. C., Pierce, J. R., Seinfeld, J. H., and Ng, N. L.: Constraining uncertainties in particle-wall deposition correction during SOA formation in chamber experiments, Atmos. Chem. Phys., 17, 2297–2310, https://doi.org/10.5194/acp-17-2297-2017, 2017.

Ng, N. L., Herndon, S. C., Trimborn, A., Canagaratna, M. R., Croteau, P. L., Onasch, T. B., Sueper, D., Worsnop, D. R., Zhang, Q., Sun, Y. L., and Jayne, J. T.: An Aerosol Chemical Speciation Monitor (ACSM) for Routine Monitoring of the Composition and Mass Concentrations of Ambient Aerosol, Aerosol Sci. Technol., 45, 780–794, https://doi.org/10.1080/02786826.2011.560211, 2011a.

Ng, N. L., Canagaratna, M. R., Jimenez, J. L., Zhang, Q., Ulbrich, I. M., and Worsnop, D. R.: Real-time methods for estimating organic component mass concentrations from aerosol mass spectrometer data, Environ. Sci. Technol., 45, 910–916, https://doi.org/10.1021/es102951k, 2011b.

Niki, H., Maker, P. D., Savage, C. M. and Breitenbach, L. P.: Fourier transform IR spectroscopic observation of chlorine nitrite, ciono, formed via $Cl + NO_2\,(+M) \rightarrow ClONO(+M)$, Chem. Phys. Lett., 59, 78–79, https://doi.org/10.1016/0009-2614(78)85618-8, 1978.

Nordmeyer, T., Wang, W., Ragains, M. L., Finlayson-Pitts, B. J., Spicer, C. W., and Plastridge, R. A.: Unique products of the reaction of isoprene with atomic chlorine: Potential markers of

chlorine atom chemistry, Geophys. Res. Lett., 24, 1615–1618, https://doi.org/10.1029/97GL01547, 1997.

Ofner, J., Kamilli, K. A., Held, A., Lendl, B., and Zetzsch, C.: Halogen-induced organic aerosol (XOA): a study on ultra-fine particle formation and time-resolved chemical characterization, Faraday Discuss., 165, 115–135, https://doi.org/10.1039/c3fd00093a, 2013.

Osthoff, H. D., Roberts, J. M., Ravishankara, A. R., Williams, E. J., Lerner, B. M., Sommariva, R., Bates, T. S., Coffman, D., Quinn, P. K., Dibb, J. E., Stark, H., Burkholder, J. B., Talukdar, R. K., Meagher, J., Fehsenfeld, F. C., and Brown, S. S.: High levels of nitryl chloride in the polluted subtropical marine boundary layer, Nat. Geosci., 1, 324–328, https://doi.org/10.1038/ngeo177, 2008.

Pankow, J. F.: An absorption model of gas/particle partitioning of organic compounds in the atmosphere, Atmos. Environ., 28, 185–188, https://doi.org/10.1016/1352-2310(94)90093-0, 1994.

Pankow, J. F. and Asher, W. E.: SIMPOL.1: a simple group contribution method for predicting vapor pressures and enthalpies of vaporization of multifunctional organic compounds, Atmos. Chem. Phys., 8, 2773–2796, https://doi.org/10.5194/acpd-7-11839-2007, 2008.

Parrish, D. D., Allen, D. T., Bates, T. S., Estes, M., Fehsenfeld, F. C., Feingold, G., Ferrare, R., Hardesty, R. M., Meagher, J. F., Nielsen-Gammon, J. W., Pierce, R. B., Ryerson, T. B., Seinfeld, J. H., and Williams, E. J.: Overview of the second texas air quality study (TexAQS II) and the Gulf of Mexico atmospheric composition and climate study (GoMACCS), J. Geophys. Res.-Atmos., 114, 1–28, https://doi.org/10.1029/2009JD011842, 2009.

Pathak, R. K., Presto, A. A., Lane, T. E., Stanier, C. O., Donahue, N. M., and Pandis, S. N.: Ozonolysis of α-pinene: parameterization of secondary organic aerosol mass fraction, Atmos. Chem. Phys., 7, 3811–3821, https://doi.org/10.5194/acp-7-3811-2007, 2007.

Patokoski, J., Ruuskanen, T. M., Hellén, H., Taipale, R., Grönholm, T., Kajos, M. K., Petäjä, T., Hakola, H., Kulmala, M., and Rinne, J.: Winter to spring transition and diurnal variation of VOCs in Finland at an urban background site and a rural site, Boreal Environ. Res., 19, 79–103, 2014.

Perraud, V., Bruns, E. A., Ezell, M. J., Johnson, S. N., Yong, Y., Alexander, M. L., Zelenyuk, A., Imre, D., Chang, W. L., Dabdub, D., Pankow, J. F., and Finlayson-Pitts, B. J.: Nonequilibrium atmospheric secondary organic aerosol formation and growth, P. Natl. Acad. Sci. USA, 109, 2836–2841, https://doi.org/10.1073/pnas.1119909109, 2012.

Presto, A. A., Miracolo, M. A., Kroll, J. H., Worsnop, D. R., Robinson, A. L., and Donahue, N. M.: Intermediate-volatility organic compounds: A potential source of ambient oxidized organic aerosol, Environ. Sci. Technol., 43, 4744–4749, https://doi.org/10.1021/es803219q, 2009.

Presto, A. A., Miracolo, M. A., Donahue, N. M., and Robinson, A. L.: Secondary organic aerosol formation from high-NOx Photooxidation of low volatility precursors: N-alkanes, Environ. Sci. Technol., 44, 2029–2034, https://doi.org/10.1021/es903712r, 2010.

Riedel, T. P., Bertram, T. H., Crisp, T. A., Williams, E. J., Lerner, B. M., Vlasenko, A., Li, S. M., Gilman, J., De Gouw, J., Bon, D. M., Wagner, N. L., Brown, S. S., and Thornton, J. A.: Nitryl chloride and molecular chlorine in the coastal marine boundary layer, Environ. Sci. Technol., 46, 10463–10470, https://doi.org/10.1021/es204632r, 2012.

Riva, M., Healy, R. M., Flaud, P. M., Perraudin, E., Wenger, J. C., and Villenave, E.: Gas- and Particle-Phase Products from the Chlorine-Initiated Oxidation of Polycyclic Aromatic Hydrocarbons, J. Phys. Chem. A, 119, 11170–11181, https://doi.org/10.1021/acs.jpca.5b04610, 2015.

Robinson, E. S., Onasch, T. B., Worsnop, D., and Donahue, N. M.: Collection efficiency of α-pinene secondary organic aerosol particles explored via light-scattering single-particle aerosol mass spectrometry, Atmos. Meas. Tech., 10, 1139–1154, https://doi.org/10.5194/amt-10-1139-2017, 2017.

Rogge, W. F., Hildemann, L. M., Mazurek, M. A., Cass, G. R., and Simoneit, B. R. T.: Sources of Fine Organic Aerosol. 3. Road Dust, Tire Debris, and Organometallic Brake Lining Dust: Roads as Sources and Sinks, Environ. Sci. Technol., 27, 1892–1904, https://doi.org/10.1021/es00046a019, 1993.

Rohrer, F., Bohn, B., Brauers, T., Brüning, D., Johnen, F.-J., Wahner, A., and Kleffmann, J.: Characterisation of the photolytic HONO-source in the atmosphere simulation chamber SAPHIR, Atmos. Chem. Phys., 5, 2189–2201, https://doi.org/10.5194/acp-5-2189-2005, 2005.

Saito, T., Kawamura, K., Nakatsuka, T., and Huebert, B. J.: In situ measurements of butane and pentane isomers over the subtropical North Pacific, Geochem. J., 38, 397–404, https://doi.org/10.2343/geochemj.38.397, 2004.

Saiz-Lopez, A. and von Glasow, R.: Reactive halogen chemistry in the troposphere, Chem. Soc. Rev., 41, 6448, https://doi.org/10.1039/c2cs35208g, 2012.

Sartelet, K. N., Couvidat, F., Seigneur, C., and Roustan, Y.: Impact of biogenic emissions on air quality over Europe and North America, Atmos. Environ., 53, 131–141, https://doi.org/10.1016/j.atmosenv.2011.10.046, 2012.

Schauer, J. J., Kleeman, M. J., Cass, G. R., and Simoneit, B. R. T.: Measurement of emissions from air pollution sources. 2. C_1 through C_{30} organic compounds from medium duty diesel trucks, Environ. Sci. Technol., 33, 1578–1587, https://doi.org/10.1021/es980081n, 1999.

Schauer, J. J., Kleeman, M. J., Cass, G. R., and Simoneit, B. R. T.: Measurement of emissions from air pollution sources. 5. C_1–C_{32} organic compounds from gasoline-powered motor vehicles, Environ. Sci. Technol., 36, 1169–1180, https://doi.org/10.1021/es0108077, 2002.

Schilling Fahnestock, K. A., Yee, L. D., Loza, C. L., Coggon, M. M., Schwantes, R., Zhang, X., Dalleska, N. F., and Seinfeld, J. H.: Secondary Organic Aerosol Composition from C_{12} Alkanes, J. Phys. Chem. A, 119, 4281–4297, https://doi.org/10.1021/jp501779w, 2015.

Schobesberger, S., D'Ambro, E. L., Lopez-Hilfiker, F. D., Mohr, C., and Thornton, J. A.: A model framework to retrieve thermodynamic and kinetic properties of organic aerosol from composition-resolved thermal desorption measurements, Atmos. Chem. Phys. Discuss., https://doi.org/10.5194/acp-2018-398, in review, 2018.

Shrivastava, M. K., Lane, T. E., Donahue, N. M., Pandis, S. N., and Robinson, A. L.: Effects of gas particle partitioning and aging of primary emissions on urban and regional organic aerosol concentrations, J. Geophys. Res.-Atmos., 113, 1–16, https://doi.org/10.1029/2007JD009735, 2008.

Simpson, W. R., Brown, S. S., Saiz-Lopez, A., Thornton, J. A., and Von Glasow, R.: Tropospheric Halogen Chemistry: Sources, Cycling, and Impacts, Chem. Rev., 115, 4035–4062, https://doi.org/10.1021/cr5006638, 2015.

Stark, H., Yatavelli, R. L. N., Thompson, S. L., Kang, H., Krechmer, J. E., Kimmel, J. R., Palm, B. B., Hu, W., Hayes, P. L., Day, D. A., Campuzano-Jost, P., Canagaratna, M. R., Jayne, J. T., Worsnop, D. R., and Jimenez, J. L.: Impact of Thermal Decomposition on Thermal Desorption Instruments: Advantage of Thermogram Analysis for Quantifying Volatility Distributions of Organic Species, Environ. Sci. Technol., 51, 8491–8500, https://doi.org/10.1021/acs.est.7b00160, 2017.

Takekawa, H., Minoura, H., and Yamazaki, S.: Temperature dependence of secondary organic aerosol formation by photooxidation of hydrocarbons, Atmos. Environ., 37, 3413–3424, https://doi.org/10.1016/S1352-2310(03)00359-5, 2003.

Tanaka, P. L., Riemer, D. D., Chang, S., Yarwood, G., McDonald-Buller, E. C., Apel, E. C., Orlando, J. J., Silva, P. J., Jimenez, J. L., Canagaratna, M. R., Neece, J. D., Mullins, C. B., and Allen, D. T.: Direct evidence for chlorine-enhanced urban ozone formation in Houston, Texas, Atmos. Environ., 37, 1393–1400, https://doi.org/10.1016/S1352-2310(02)01007-5, 2003.

Thompson, S. L., Yatavelli, R. L. N., Stark, H., Kimmel, J. R., Krechmer, J. E., Day, D. A., Hu, W., Isaacman-VanWertz, G., Yee, L., Goldstein, A. H., Khan, M. A. H., Holzinger, R., Kreisberg, N., Lopez-Hilfiker, F. D., Mohr, C., Thornton, J. A., Jayne, J. T., Canagaratna, M., Worsnop, D. R., and Jimenez, J. L.: Field intercomparison of the gas/particle partitioning of oxygenated organics during the Southern Oxidant and Aerosol Study (SOAS) in 2013, Aerosol Sci. Technol., 51, 30–56, https://doi.org/10.1080/02786826.2016.1254719, 2017.

Thornton, J. A., Kercher, J. P., Riedel, T. P., Wagner, N. L., Cozic, J., Holloway, J. S., Dubé, W. P., Wolfe, G. M., Quinn, P. K., Middlebrook, A. M., Alexander, B., and Brown, S. S.: A large atomic chlorine source inferred from mid-continental reactive nitrogen chemistry, Nature, 464, 271–274, https://doi.org/10.1038/nature08905, 2010.

Tkacik, D. S., Presto, A. A., Donahue, N. M., and Robinson, A. L.: Secondary organic aerosol formation from intermediate-volatility organic compounds: Cyclic, linear, and branched alkanes, Environ. Sci. Technol., 46, 8773–8781, https://doi.org/10.1021/es301112c, 2012.

Ulbrich, I. M., Canagaratna, M. R., Zhang, Q., Worsnop, D. R., and Jimenez, J. L.: Interpretation of Organic Components from Positive Matrix Factorization of Aerosol Mass Spectrometric Data, Atmos. Chem. Phys., 9, 2891, https://doi.org/10.5194/acp-9-2891-2009, 2009.

Veres, P. R., Roberts, J. M., Wild, R. J., Edwards, P. M., Brown, S. S., Bates, T. S., Quinn, P. K., Johnson, J. E., Zamora, R. J., and de Gouw, J.: Peroxynitric acid (HO2NO2) measurements during the UBWOS 2013 and 2014 studies using iodide ion chemical ionization mass spectrometry, Atmos. Chem. Phys., 15, 8101–8114, https://doi.org/10.5194/acp-15-8101-2015, 2015.

Wang, D. S. and Hildebrandt Ruiz, L.: Secondary organic aerosol from chlorine-initiated oxidation of isoprene, Atmos. Chem. Phys., 17, 13491–13508, https://doi.org/10.5194/acp-17-13491-2017, 2017.

Wang, M., Yao, L., Zheng, J., Wang, X., Chen, J., Yang, X., Worsnop, D. R., Donahue, N. M., and Wang, L.: Reactions of Atmospheric Particulate Stabilized Criegee Intermediates Lead to High-Molecular-Weight Aerosol Components, Environ. Sci. Technol., 50, 5702–5710, https://doi.org/10.1021/acs.est.6b02114, 2016.

Xu, W., Lambe, A., Silva, P., Hu, W., Onasch, T., Williams, L., Croteau, P., Zhang, X., Renbaum-Wolff, L., Fortner, E., Jimenez, J. L., Jayne, J., Worsnop, D., and Canagaratna, M.: Laboratory evaluation of species-dependent relative ionization efficiencies in the Aerodyne Aerosol Mass Spectrometer, Aerosol Sci. Technol., 52, 626–641, https://doi.org/10.1080/02786826.2018.1439570, 2018.

Yee, L. D., Craven, J. S., Loza, C. L., Schilling, K. A., Ng, N. L., Canagaratna, M. R., Ziemann, P. J., Flagan, R. C., and Seinfeld, J. H.: Secondary Organic Aerosol Formation from Low-NO_x Photooxidation of Dodecane: Evolution of Multigeneration Gas-Phase Chemistry and Aerosol Composition, J. Phys. Chem. A, 116, 6211–6230, https://doi.org/10.1021/jp211531h, 2012.

Yee, L. D., Craven, J. S., Loza, C. L., Schilling, K. A., Ng, N. L., Canagaratna, M. R., Ziemann, P. J., Flagan, R. C., and Seinfeld, J. H.: Effect of chemical structure on secondary organic aerosol formation from C_{12} alkanes, Atmos. Chem. Phys., 13, 11121–11140, https://doi.org/10.5194/acp-13-11121-2013, 2013.

Yeh, G. K. and Ziemann, P. J.: Alkyl nitrate formation from the reactions of C_8-C_{14}n-Alkanes with OH radicals in the presence of NO_x: Measured yields with essential corrections for gas-wall partitioning, J. Phys. Chem. A, 118, 8147–8157, https://doi.org/10.1021/jp500631v, 2014.

Yeh, G. K. and Ziemann, P. J.: Gas-Wall Partitioning of Oxygenated Organic Compounds: Measurements, Structure-Activity Relationships, and Correlation with Gas Chromatographic Retention Factor, Aerosol Sci. Technol., 6826, 727–738, https://doi.org/10.1080/02786826.2015.1068427, 2015.

Young, C. J., Washenfelder, R. A., Edwards, P. M., Parrish, D. D., Gilman, J. B., Kuster, W. C., Mielke, L. H., Osthoff, H. D., Tsai, C., Pikelnaya, O., Stutz, J., Veres, P. R., Roberts, J. M., Griffith, S., Dusanter, S., Stevens, P. S., Flynn, J., Grossberg, N., Lefer, B., Holloway, J. S., Peischl, J., Ryerson, T. B., Atlas, E. L., Blake, D. R., and Brown, S. S.: Chlorine as a primary radical: Evaluation of methods to understand its role in initiation of oxidative cycles, Atmos. Chem. Phys., 14, 3427–3440, https://doi.org/10.5194/acp-14-3427-2014, 2014.

Zavala-Araiza, D., Lyon, D. R., Alvarez, R. A., Davis, K. J., Harriss, R., Herndon, S. C., Karion, A., Kort, E. A., Lamb, B. K., Lan, X., Marchese, A. J., Pacala, S. W., Robinson, A. L., Shepson, P. B., Sweeney, C., Talbot, R., Townsend-Small, A., Yacovitch, T. I., Zimmerle, D. J., and Hamburg, S. P.: Reconciling divergent estimates of oil and gas methane emissions, P. Natl. Acad. Sci. USA, 112, 22126, https://doi.org/10.1073/pnas.1522126112, 2015.

Zavala-Araiza, D., Alvarez, R. A., Lyon, D. R., Allen, D. T., Marchese, A. J., Zimmerle, D. J., and Hamburg, S. P.: Super-emitters in natural gas infrastructure are caused by abnormal process conditions, Nat. Commun., 8, 14012, https://doi.org/10.1038/ncomms14012, 2017.

Zhang, Q., Jimenez, J. L., Canagaratna, M. R., Allan, J. D., Coe, H., Ulbrich, I., Alfarra, M. R., Takami, A., Middlebrook, A. M., Sun, Y. L., Dzepina, K., Dunlea, E., Docherty, K., DeCarlo, P. F., Salcedo, D., Onasch, T., Jayne, J. T., Miyoshi, T., Shimono, A., Hatakeyama, S., Takegawa, N., Kondo, Y., Schneider, J., Drewnick, F., Borrmann, S., Weimer, S., Demer-

jian, K., Williams, P., Bower, K., Bahreini, R., Cottrell, L., Griffin, R. J., Rautiainen, J., Sun, J. Y., Zhang, Y. M., and Worsnop, D. R.: Ubiquity and dominance of oxygenated species in organic aerosols in anthropogenically-influenced Northern Hemisphere midlatitudes, Geophys. Res. Lett., 34, L13801, https://doi.org/10.1029/2007GL029979, 2007.

Zhang, X., Schwantes, R. H., Coggon, M. M., Loza, C. L., Schilling, K. A., Flagan, R. C., and Seinfeld, J. H.: Role of ozone in SOA formation from alkane photooxidation, Atmos. Chem. Phys., 14, 1733–1753, https://doi.org/10.5194/acp-14-1733-2014, 2014.

Ziemann, P. J.: Effects of molecular structure on the chemistry of aerosol formation from the OH-radical-initiated oxidation of alkanes and alkenes, Int. Rev. Phys. Chem., 30, 161–195, https://doi.org/10.1080/0144235X.2010.550728, 2011.

Supplement of Atmos. Chem. Phys., 18, 15535–15553, 2018
https://doi.org/10.5194/acp-18-15535-2018-supplement

Atmospheric Chemistry and Physics
Open Access
EGU

Supplement of

Chlorine-initiated oxidation of n-alkanes under high-NO_x conditions: insights into secondary organic aerosol composition and volatility using a FIGAERO–CIMS

Dongyu S. Wang and Lea Hildebrandt Ruiz

Correspondence to: Lea Hildebrandt Ruiz (lhr@che.utexas.edu)

S1 Additional Table and Figures

Table S1. SOA Bulk Composition and Alternative Yields

Exp #	Precursors	RH	Y_{SOA}[a]	MW[b]	$Y_{SOA,m}$[c]	ρ[d]	$Y_{SOA,L}$[e]	$f_{HCl,A}$[f]	$f_{Cl,F}$[g]	f_{OCl}[h]	f_{ON}[i]	R_{ON}[j]
1	Octane, NO, Cl_2	5 >	0.28	226	0.14	2.3	0.13	1.3 E^{-2}	1.8 E^{-2}	0.15	0.54	0.64
2	Octane, NO_2, Cl_2	5 >	0.16	223	0.08	1.7	0.10	1.1 E^{-2}	1.7 E^{-2}	0.14	0.49	0.57
3	Octane, NO, NO_2, Cl_2	5 >	0.24	206	0.13	1.8	0.14	1.0 E^{-2}	2.1 E^{-2}	0.15	0.49	0.57
4	Octane, NO, NO_2, Cl_2	35	0.24	223	0.12	2.1	0.12	1.4 E^{-2}	1.9 E^{-2}	0.14	0.49	0.57
5	Decane, NO, Cl_2	5 >	0.84	265	0.45	2.3	0.39	1.1 E^{-2}	1.5 E^{-2}	0.13	0.60	0.84
6	Decane, NO_2, Cl_2	5 >	0.45	249	0.26	2.0	0.24	1.0 E^{-2}	1.6 E^{-2}	0.14	0.56	0.75
7	Decane, NO, NO_2, Cl_2	5 >	0.80	241	0.47	2.1	0.40	1.2 E^{-2}	1.6 E^{-2}	0.12	0.59	0.75
8	Decane, NO, NO_2, Cl_2	40	0.50	243	0.29	1.6	0.33	1.2 E^{-2}	1.7 E^{-2}	0.13	0.56	0.71
9	Dodecane, NO, Cl_2	5 >	1.65	270	1.04	1.8	0.99	0.8 E^{-2}	1.7 E^{-2}	0.14	0.67	0.93
10	Dodecane, NO_2, Cl_2	5 >	1.25	258	0.82	2.1	0.63	1.4 E^{-2}	1.7 E^{-2}	0.14	0.60	0.78
11	Dodecane, NO, NO_2, Cl_2	5 >	1.40	264	0.90	2.4	0.62	1.4 E^{-2}	1.8 E^{-2}	0.15	0.62	0.82
12	Dodecane, NO, NO_2, Cl_2	67	1.10	260	0.72	2.4	0.49	1.1 E^{-2}	1.6 E^{-2}	0.13	0.61	0.77

(a) Assuming a CE of 0.5 and RIE of 1.4 for ACSM, in μg m^{-3}

(b) Average molecular weight calculated based on organic ions (I^- adducts only) observed by FIGAERO-CIMS in g mol^{-1}

(c) SOA molar yield, calculated using Eqs. S1-3, in mol mol^{-1}

(d) Density calculated based ACSM mass measurements and SEMS volume measurements

(e) SOA mass yield, recalculated assuming the lowest reported alkane-OH density, 1.06 g cm^{-3} (Lim and Ziemann, 2009), in μg m^{-3}

(f) Mass fraction of -Cl functional group, estimated using the ACSM measurement of HCl^+ ion, relative to the bulk SOA

(g) Mass fraction of -Cl functional group, estimated using the SOA molecular composition as measured by the FIGAERO-CIMS, relative to the total organic ions observed

(h) Mass fraction of organochlorides (including chloronitrates), estimated using the SOA molecular composition as measured by the FIGAERO-CIMS, relative to the total organic ions observed

(i) Mass fraction of organonitrates (excluding chloronitrates), estimated using the SOA molecular composition as measured by the FIGAERO-CIMS, relative to the total organic ions observed

(j) Average ratio of $-NO_3$ functional group to the number of carbon, estimated using the SOA molecular composition as measured by the FIGAERO-CIMS. Individual $-NO_3$ functional groups in dinitrates and trinitrates are counted separately (e.g. a C_{12} dinitrate has the same R_{ON} as a C_6 mononitrate).

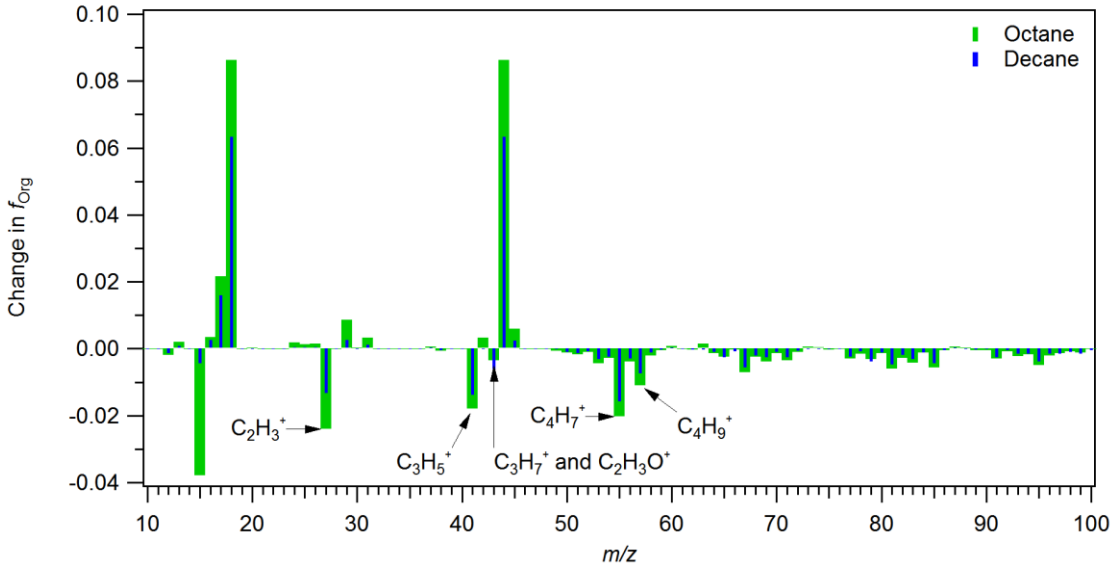

Figure S1: Change in the fractional contribution by different organic ion fragments to the overall organic aerosol mass as measured by the ACSM. Dodecane-Cl SOA (Exp. 11) was used as the reference for octane-Cl SOA (Exp. 3) and decane-Cl SOA (Exp. 7) produced under similar oxidation conditions under low RH. Mass spectra shown are 50-minute averages from minute 10 to 60 during the photooxidation period. Ion identities indicated ($C_2H_3^+$, $C_3H_5^+$, $C_3H_7^+$, $C_2H_3O^+$, $C_4H_7^+$, $C_4H_9^+$) were assumed, as the quadruple ACSM used lacks the necessary mass resolution for exact identification. At *m/z* 43, the $C_2H_3O^+$ is expected to dominate. Highlighted C_xH_y ions are often associated with hydrocarbon-like organic aerosol (Ng et al., 2011; Ulbrich et al., 2009). Clear enhancement of *m/z* 44 and associated ion fragments (e.g. *m/z* 16, 17, and 18) was also observed for octane and decane SOA.

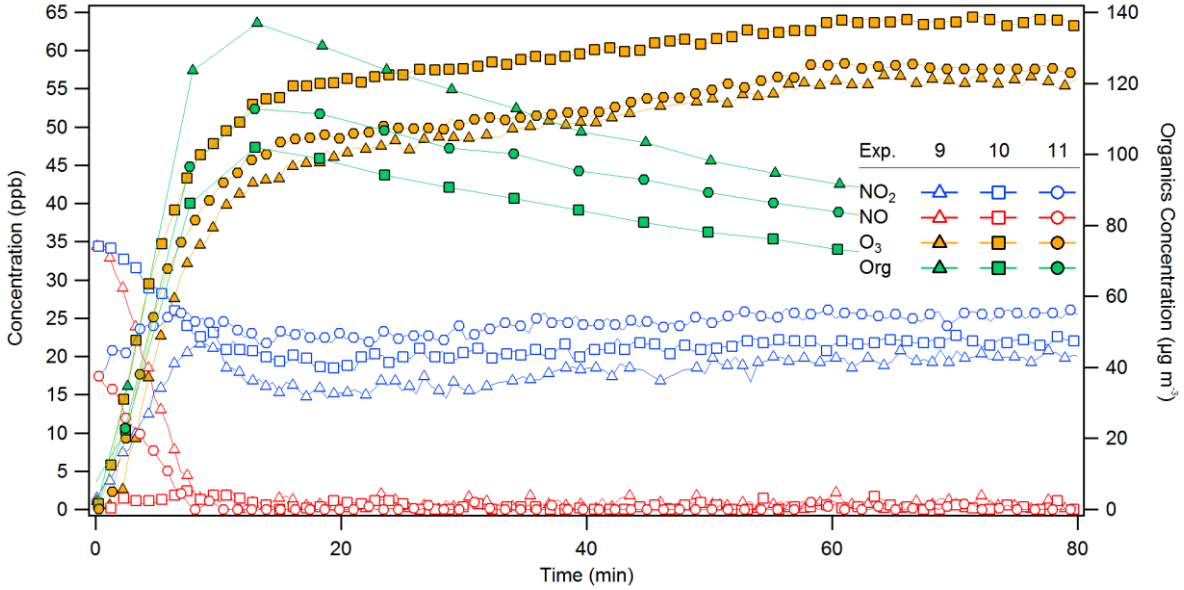

Figure S2: Example of NO, NO_2, O_3 and SOA trends under different starting NO_x conditions. Exp. 9 (high initial NO), 10 (high initial NO_2), and 11 (balanced initial NO and NO_2) for chlorine-initiated oxidation of dodecane under low RH conditions are shown. Ozone production slowed down significantly as the NO_x concentrations plateaued and as the SOA concentrations approached their maxima. By the end of the photooxidation period (60 min), lowest final NO_x concentrations (consisting of NO_2 and interferences, which may include alkyl nitrates) and highest SOA concentrations were observed for high initial NO concentrations (Exp. 1 for octane, Exp. 5 for decane, and Exp. 9 for dodecane).

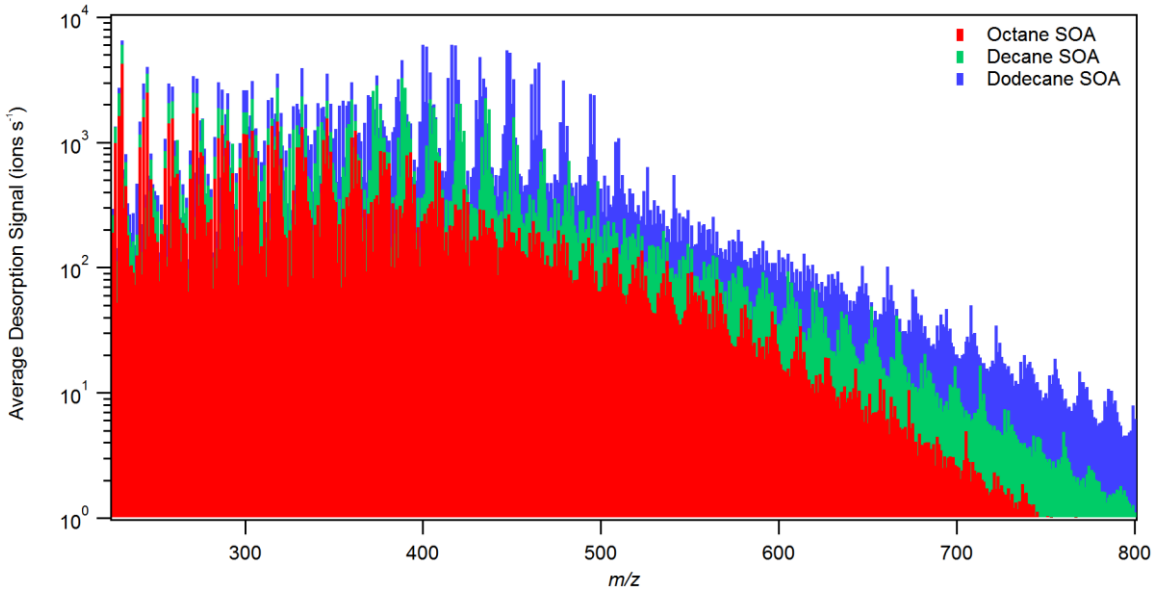

Figure S3: Comparison of particle-phase composition during FIGAERO desorption for octane (Exp. 3), decane (Exp. 7), and dodecane (Exp. 11). Same as Figure 4 in the main text but with the y-axis in logarithmic scale and the x-axis (*m/z*) extended to the maximum sampled range. Desorption signals are not stacked.

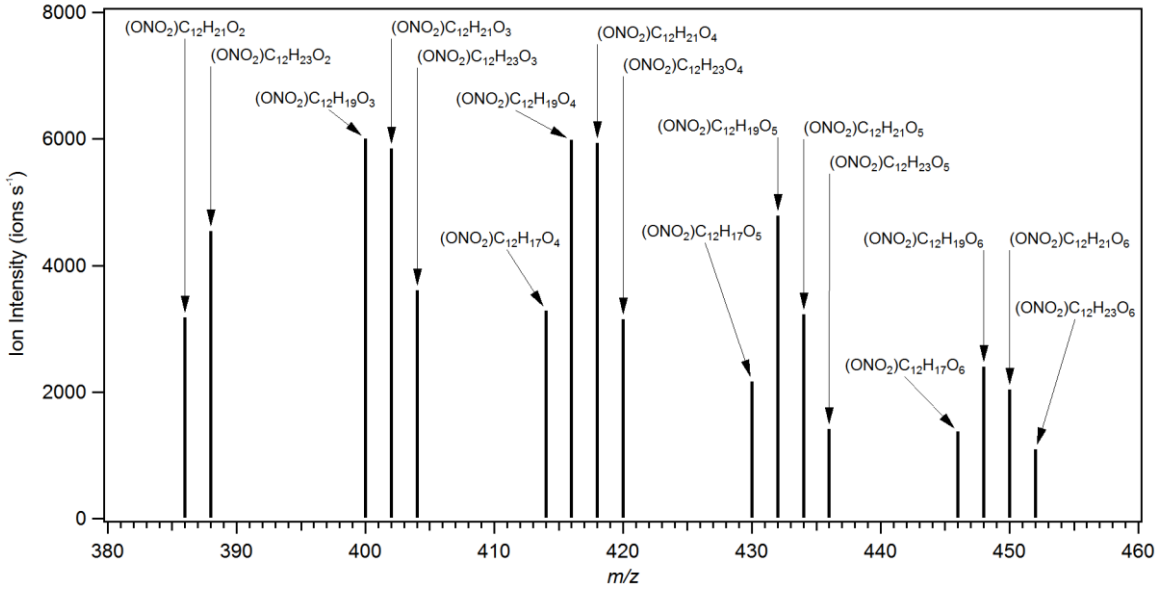

Figure S4: Particle-phase distribution of C_{12} organic (mono-)nitrates. Assuming equal sensitivity, the particle-phase abundance roughly followed a bell-shape distribution across the different oxygenation groups, peaking at the O_3 or O_4 group. Within each oxygenation group, the product distribution follows a bell-shape around H_{19} and H_{21} compounds. Similar bell-shaped organic nitrate distribution has been observed for ambient isoprene- and monoterpene-derived organonitrates (Lee et al., 2016).

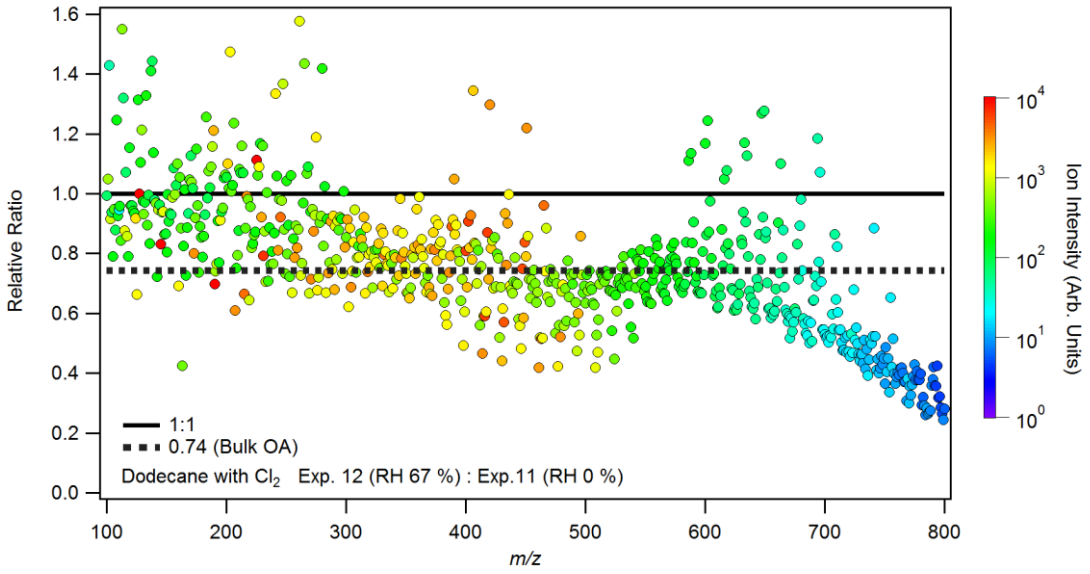

Figure S5: Ratio of integrated unit-mass resolution FIGAERO-CIMS desorption signal during temperature ramp from a high-RH SOA formation experiment (Exp. 12, 67 % RH) to that from a low-RH SOA formation experiment (Exp. 11, < 5 % RH). Integrated ion intensity is shown on a logarithmic scale as the color. The ratio of bulk organics concentration during the filter collection period calculated using ACSM data is shown as the dotted black line. Except for the low molecular weight thermal fragmentation/decomposition products and the high molecular weight, low-volatility compounds, the unit-mass ion ratios appear in agreement with bulk measurement. Under high RH conditions, the higher molecular weight (m/z > 600) compounds become increasingly suppressed.

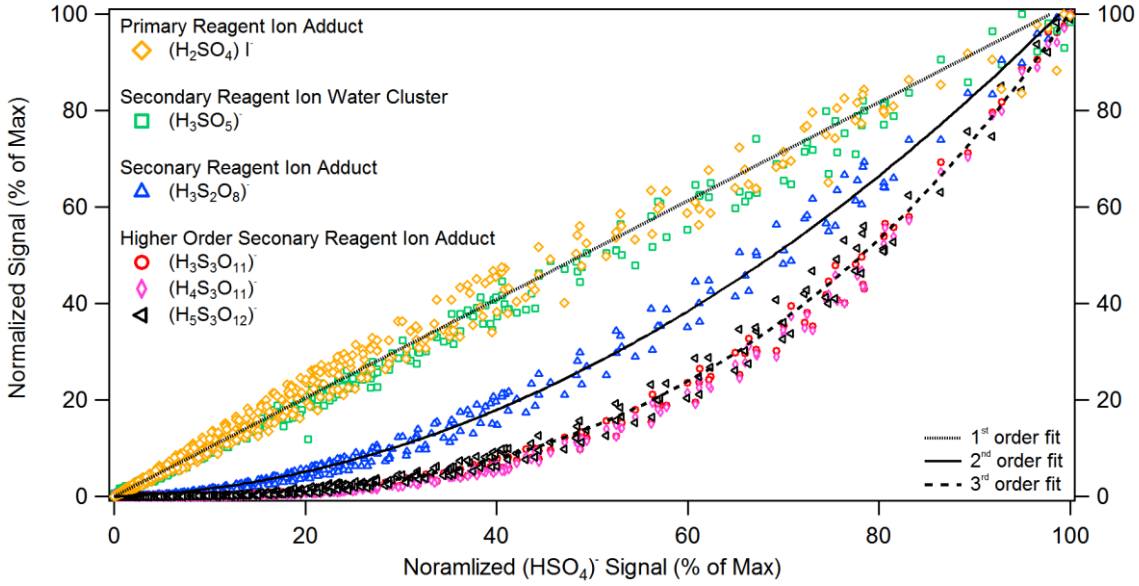

Figure S6: Example of secondary HSO_4^- ionization products. Ion signals observed during $(NH_4)_2SO_4$ thermal decomposition were first normalized by I^- signal and then normalized against the maximum desorption signal observed for each ion. Linear (1st order), quadratic (2nd order), and cubic equations (3rd order) are fitted.

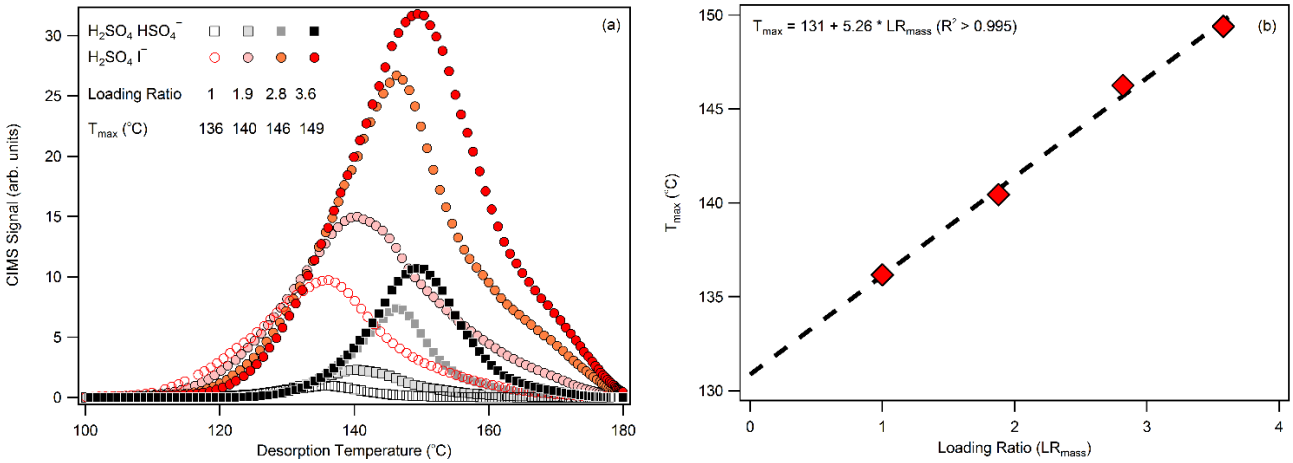

Figure S7: The 1-D thermograms for two $(NH_4)_2SO_4$ decomposition product ions. $H_2SO_4 \bullet I^-$ was the primary adduct and $H_2SO_4 \bullet HSO_4^-$ was a secondary ionization product. The lowest time-integrated desorption ion intensity for H_2SO_4 I^- was used as the basis for calculating the loading ratio (LR_{mass}). The loading ratio for $H_2SO_4 \bullet HSO_4^-$ (not shown) is the square of that for H_2SO_4 I^- (b) Linear regression fitting of T_{max} as a function of the LR_{mass}. T_{max} increased linearly with mass loading of $(NH_4)_2SO_4$.

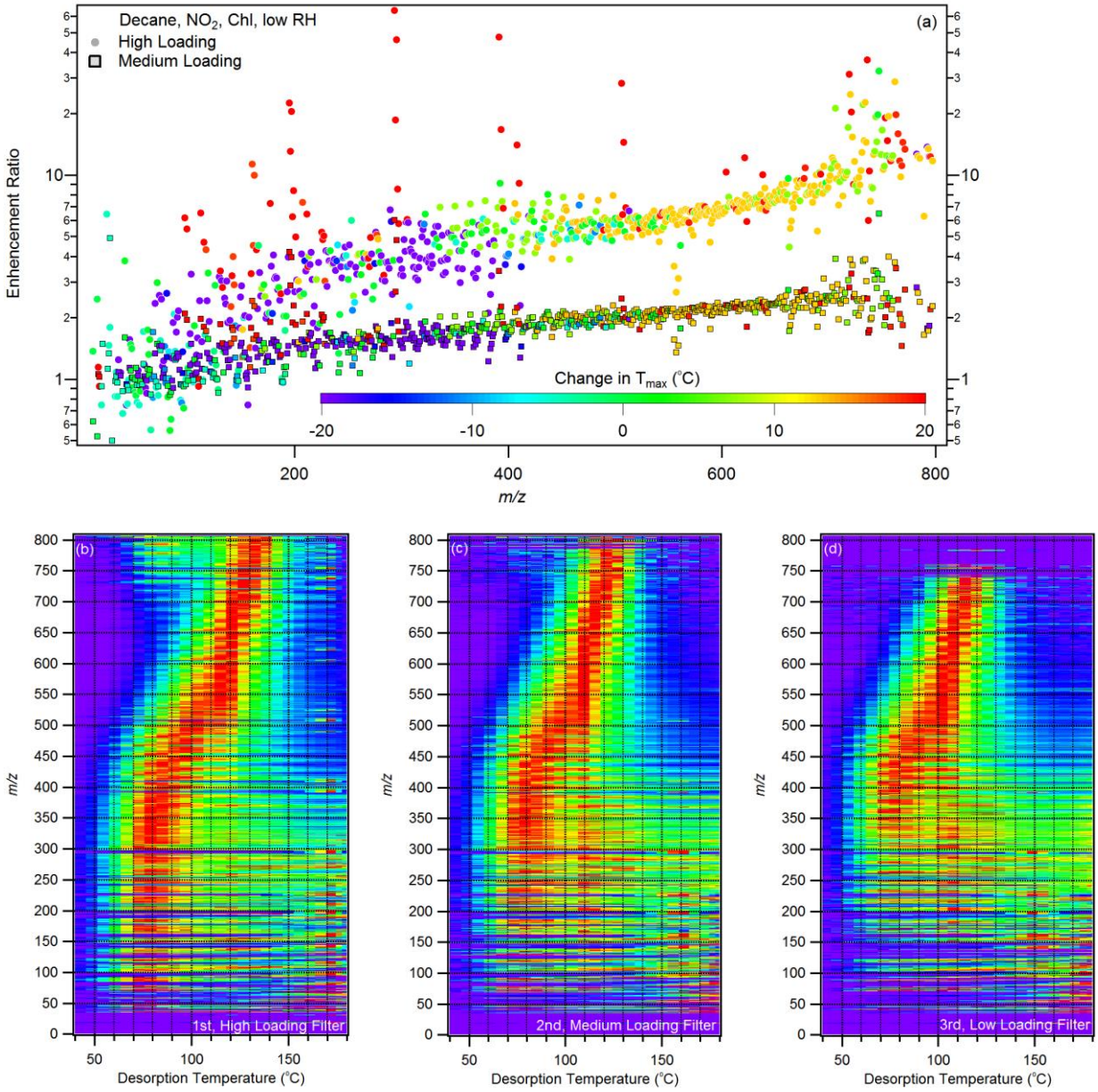

Figure S8: Effects of aerosol loading on T_{max}. Three SOA filter samples were collected during Exp. 6 for 45 mins, 30 mins, and 15 mins, in that order. Each filter was subjected to two full desorption runs to minimize carry-over effects and to determine the filter background. (a) Enhancement ratios calculated using unit-mass integrated signals for the lowest filter loading run as the referenced condition. Color scale shows T_{max} shifts in °C, using the T_{max} values observed in the low loading run as the reference point. (b) 2-D thermogram for the first, high loading filter, (c) for the second, medium loading filter, and for (d) the third, low loading filter. For (b-d), the color scale represents the normalized desorption intensity as a percentage of the maximum, same as in Fig. 5 in the main text. Between the time it took for filter collection and filter desorption, the ion intensity of some high molecular weight, low volatility compounds had decreased to below the limits of detection (i.e. 3σ of the background signal) in the particle phase, likely due to volatility-dependent wall loss. Disappearance of low *m/z* (< 300) compounds maybe due to decreases in suspended aerosol concentration, making it unfavorable for semi-volatile compounds to partition to the particle phase, or may be associated with the loss of high molecular weight oligomers, assuming that the low *m/z* desorption ions were dominated by low-temperature (T_{max} < ~80 °C) thermal fragmentation products as opposed to semi-volatile monomers.

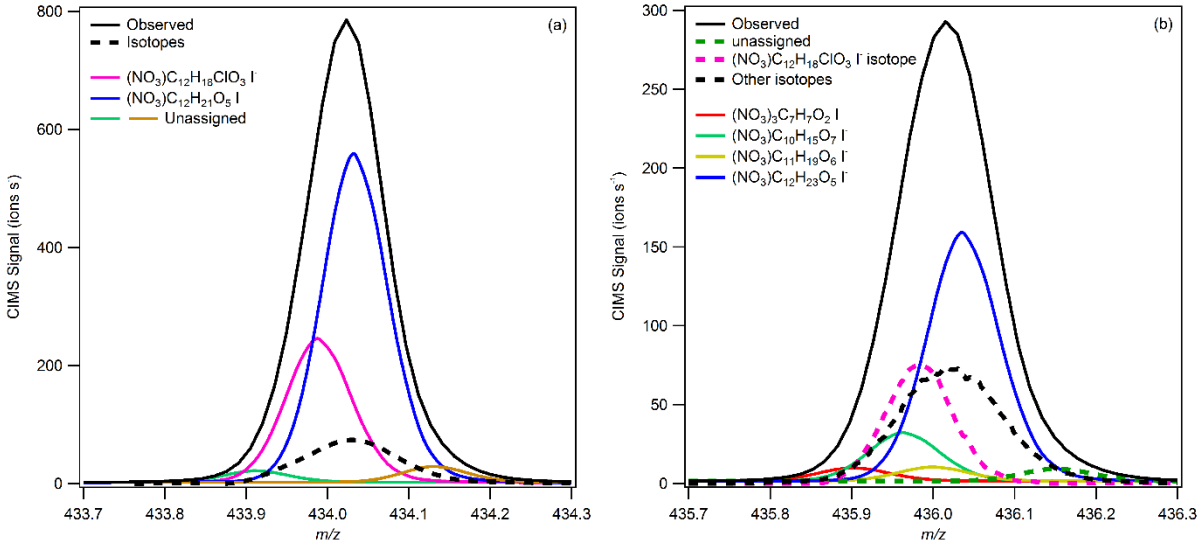

Figure S9: High resolution fitting at *m/z* (a) 434 and (b) 436 for FIGAERO-CIMS data from Exp. 11. The C_{12} chloronitrate (ONO_2-$C_{12}H_{18}ClO_3$•I^-) peak is tentatively identified in (a) but it overlaps with the nearby stronger organonitrate (ONO_2-$C_{12}H_{21}O_5$•I^-) peak. Because the chloronitrate peak is a weaker peak with significant overlap with a stronger peak, quantitative assessment would be challenging due to peak fitting uncertainties (Cubison and Jimenez, 2015). The presence of chloronitrate cannot be confirmed or rejected based on its unique isotopic signature at *m/z*+2 positions, as shown in (b), where nonchlorinated compounds also dominate.

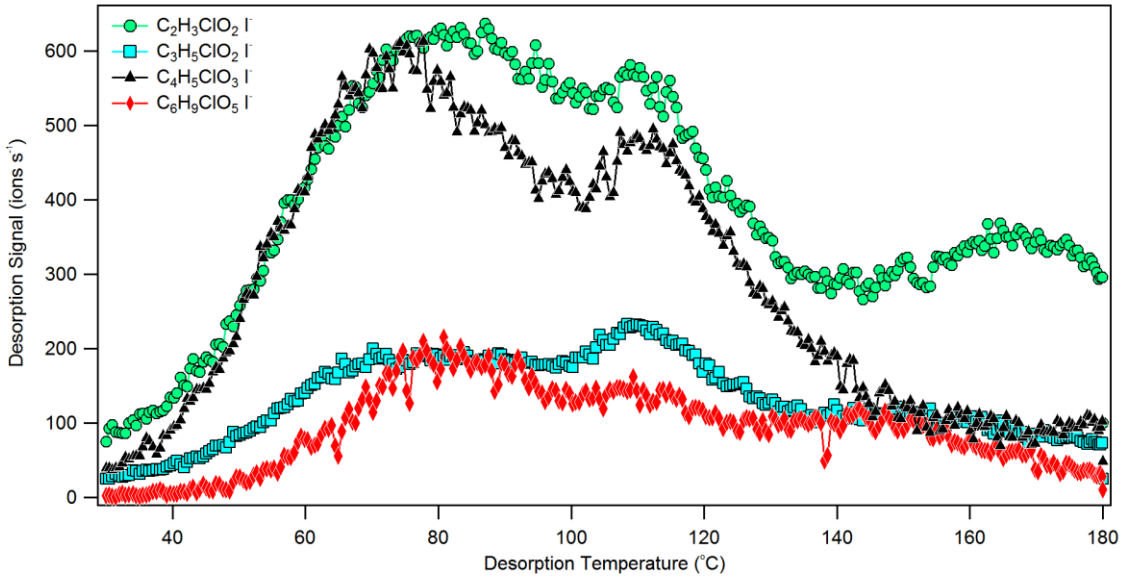

Figure S10: 1-D thermogram of select organochlorides observed for Exp 10. All compounds shown exhibited multimodal desorption behaviors. $C_2H_3ClO_2$ is too volatile to be present as a molecular compound in the particle phase and is therefore a thermal decomposition product. $C_2H_3ClO_2$ shows three local maxima at ~87 ºC, ~109 ºC, and ~167 ºC. The T_{max} for the least volatile desorption mode of $C_2H_3ClO_2$ is higher than that for ammonium sulfate seed particles (~155 ºC) from the same filter run, and may be produced from thermal decomposition of extremely low volatility organochlorides. However, larger organochloride ions were not observed to have any distinct T_{max} modes over these very high temperature ranges (> 160 ºC)

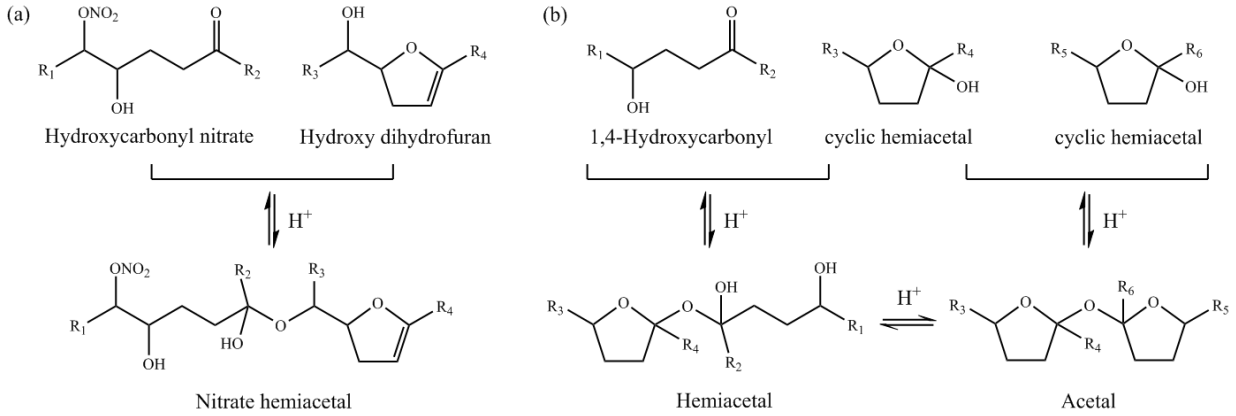

Figure S11: Oligomerization via the reaction between (a) carbonyl hydroxyl nitrate and hydroxy dihydrofuran proposed by Schilling Fahnestock et al. (2015) and (b) cyclic hemiacetal with either a 1,4-hydroxycarbonyl or another cyclic hemiacetal proposed by Aimanant and Ziemann (2013). Condensed-phase isomerization between acetal and hemiacetal dimers is also possible, as shown in (b).

S2. Interaction between Cl, NO_x, and HO_x

Formation of HO_2NO_2 likely proceeds via

$$HO_2 + NO_2 \xrightarrow{M} HO_2NO_2 \qquad \text{R. (S1)}$$

Formation of HONO under UV can proceed via

$$HO_2 + NO \rightarrow OH + NO_2 \qquad \text{R. (S2)}$$
$$OH + NO \rightarrow HONO \qquad \text{R. (S3)}$$

The trends for HO_2NO_2, HONO, and select gas-phase species observed by the I^- CIMS are shown in Fig. S12.

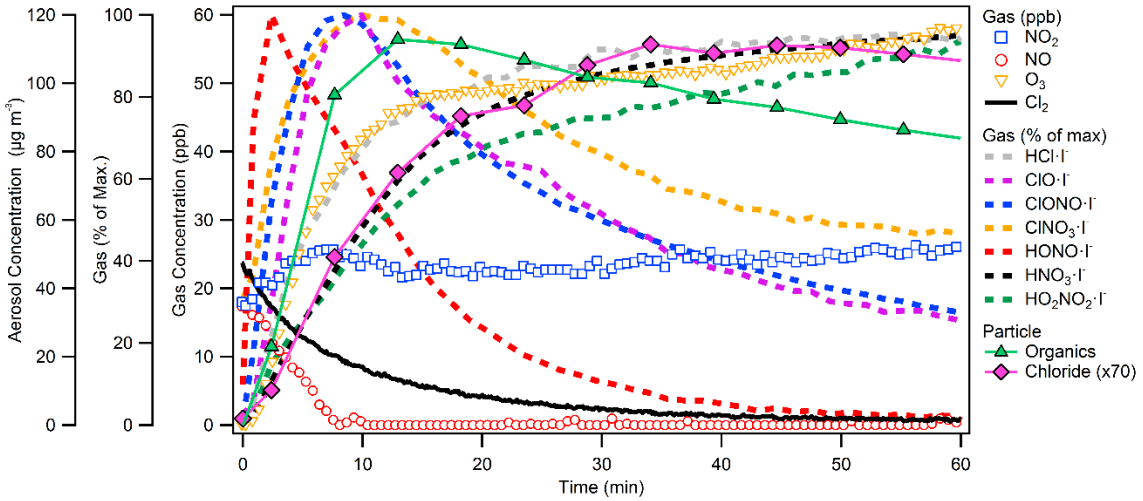

Figure S12: Representative trends of SOA and trace gas species during the photooxidation period. Data from dodecane oxidation (Exp. 11) are shown, similar to Fig. 1 in the main text. Additional species shown include $ClONO_2$ (from reaction between ClONO with NO_2, Lesar et al., 2006), ClO (possibly a ion fragment of ClONO), HCl (from H-abstraction by $Cl^•$ or perhaps Cl-elimination reactions), and HNO_3 (due to the oxidation of NO_2 by OH).

S3. Calculation of Bulk SOA Properties using the FIGAERO-CIMS

If equal sensitivity is assumed for all ions (i.e. I^- adducts detected by the FIGAERO-CIMS), the average molecular weight, mw_{avg} is estimated based on the (desorption) intensity I_i and the molecular weight, mw_i of all ions identified,

$$mw_{avg}(T_d) = \frac{\sum_i mw_i \times I_i(T_d)}{\sum_i I_i(T_d)} \qquad \text{Eq. (S1)}$$

where mw_{avg} and I_i vary with desorption temperature, T_d during a single FIGAERO desorption. A single average molecular weight for the entire FIGAERO desorption run can be calculated based on the integrated values over the T_d range,

$$mw_{SOA} = \frac{\int(\sum_i mw_i \times I_i(T_d))\Delta T_d}{\int(\sum_i I_i(T_d))\Delta T_d} \qquad \text{Eq. (S2)}$$

where ΔT_d is the step change in desorption temperature. It should be noted that because of thermal decomposition, which has also been observed for monomers (Stark et al., 2017), the mw_{avg} and mw_{SOA} calculated using the FIGAERO-CIMS data likely underestimate the actual average SOA molecular weight. For octane SOA, mw_{SOA} calculated in this way ranges from 206 to

226 g mol^{-1}; for decane SOA, mw_{SOA} ranges from 241 to 265 g mol^{-1}; for dodecane SOA, mw_{SOA} ranges from 260 to 270 g mol^{-1}. The molar SOA yield can then be calculated as,

$$Y_{molar} = \frac{n_{SOA}}{\Delta n_{VOC}} = \frac{m_{SOA}/mw_{SOA}}{\Delta m_{VOC}/mw_{VOC}} = Y\frac{mw_{VOC}}{mw_{SOA}} \quad \text{Eq. (S3)}$$

where n_{SOA} and n_{VOC} are the molar concentrations of SOA and VOC. The molecular weight of VOC, mw_{VOC} is known for the alkane precursors. The corresponding molar yield ranges from 0.08 to 0.14 for octane SOA, 0.26 to 0.47 for decane SOA, and 0.72 to 1.04 for dodecane SOA. The above-unity molar SOA yield observed for dodecane (Exp. 9) indicates that SOA mass may be overestimated, which may be the result of uncertainties with the collection efficiency (CE) and relative ionization efficiency (RIE) assumed for the SOA.

Equations S1 and S2 can also be used to calculate various other bulk SOA properties, including elemental ratios such as the oxygen-to-carbon ratio (O:C), hydrogen-to-carbon ratio (H:C), nitrate-to-carbon ratio (NO_3:C), chloride-to-carbon ratio (Cl:C), or the oxidation state of carbon (OS_C). Using the oxygen-to-carbon ratio (O:C) as the example, the bulk SOA elemental ratios as a function of the FIGAERO desorption temperature, T_d can be calculated as

$$O{:}C_{avg}(T_d) = \frac{n_O(T_d)}{n_C(T_d)} = \frac{\sum_i n_{O,i}\times I_i(T_d)}{\sum_i n_{C,i}\times I_i(T_d)} \quad \text{Eq. (S4)}$$

where n_O is the total number of oxygen atoms present in the desorbed ions at T_d, n_C is the total number of carbon atoms, $n_{O,i}$ is the number of oxygen atom present in compound *i* as determined by its assigned molecular formula (which is independent of T_d), $n_{C,i}$ is the number of carbon present in compound *i*, and I_i is the desorption ion intensity for compound *i* at T_d. Equal sensitivity is assume for ions used for the analysis such that I_i can be used as the molar amount for compound *i*.

References

Aimanant, S. and Ziemann, P. J.: Chemical mechanisms of aging of aerosol formed from the reaction of n-pentadecane with OH radicals in the presence of NOx, Aerosol Sci. Technol., 47(9), 979–990, doi:10.1080/02786826.2013.804621, 2013.

Cubison, M. J. and Jimenez, J. L.: Statistical precision of the intensities retrieved from constrained fitting of overlapping peaks in high-resolution mass spectra, Atmos. Meas. Tech., 8(6), 2333–2345, doi:10.5194/amt-8-2333-2015, 2015.

Hu, W., Campuzano-Jost, P., Day, D. A., Croteau, P., Canagaratna, M. R., Jayne, J. T., Worsnop, D. R. and Jimenez, J. L.: Evaluation of the new capture vaporizer for aerosol mass spectrometers (AMS) through field studies of inorganic species, Aerosol Sci. Technol., 51(6), 735–754, doi:10.1080/02786826.2017.1296104, 2017.

Lee, B. H., Mohr, C., Lopez-Hilfiker, F. D., Lutz, A., Hallquist, M., Lee, L., Romer, P., Cohen, R. C., Iyer, S., Kurtén, T., Hu, W., Day, D. A., Campuzano-Jost, P., Jimenez, J. L., Xu, L., Ng, N. L., Guo, H., Weber, R. J., Wild, R. J., Brown, S. S., Koss, A., de Gouw, J., Olson, K., Goldstein, A. H., Seco, R., Kim, S., McAvey, K., Shepson, P. B., Starn, T., Baumann, K., Edgerton, E. S., Liu, J., Shilling, J. E., Miller, D. O., Brune, W., Schobesberger, S., D'Ambro, E. L. and Thornton, J. A.: Highly functionalized organic nitrates in the southeast United States: Contribution to secondary organic aerosol and reactive nitrogen budgets, Proc. Natl. Acad. Sci., 113(6), 201508108, doi:10.1073/pnas.1508108113, 2016.

Lesar, A., Kovačič, S. and Hodošček, M.: ClONO and BrONO loss mechanisms in the presence of NO2: A quantum-mechanical study, Chem. Phys. Lett., 429(4–6), 343–349, doi:10.1016/j.cplett.2006.07.058, 2006.

Lim, Y. B. and Ziemann, P. J.: Effects of molecular structure on aerosol yields from OH radical-initiated reactions of linear, branched, and cyclic alkanes in the presence of NO x, Environ. Sci. Technol., 43(7), 2328–2334, doi:10.1021/es803389s, 2009.

Ng, N. L., Canagaratna, M. R., Jimenez, J. L., Zhang, Q., Ulbrich, I. M. and Worsnop, D. R.: Real-time methods for estimating organic component mass concentrations from aerosol mass spectrometer data, Environ. Sci. Technol., 45(3), 910–916, doi:10.1021/es102951k, 2011.

Schilling Fahnestock, K. A., Yee, L. D., Loza, C. L., Coggon, M. M., Schwantes, R., Zhang, X., Dalleska, N. F. and Seinfeld, J. H.: Secondary Organic Aerosol Composition from C $_{12}$ Alkanes, J. Phys. Chem. A, 119(19), 4281–4297, doi:10.1021/jp501779w, 2015.

Stark, H., Yatavelli, R. L. N., Thompson, S. L., Kang, H., Krechmer, J. E., Kimmel, J. R., Palm, B. B., Hu, W., Hayes, P. L., Day, D. A., Campuzano-Jost, P., Canagaratna, M. R., Jayne, J. T., Worsnop, D. R. and Jimenez, J. L.: Impact of Thermal Decomposition on Thermal Desorption Instruments: Advantage of Thermogram Analysis for Quantifying Volatility Distributions of Organic Species, Environ. Sci. Technol., 51(15), 8491–8500, doi:10.1021/acs.est.7b00160, 2017.

Ulbrich, I. M., Canagaratna, M. R., Zhang, Q., Worsnop, D. R. and Jimenez, J. L.: Interpretation of Organic Components from Positive Matrix Factorization of Aerosol Mass Spectrometric Data., Atmos. Chem. Phys., 9, 2891, doi:10.5194/acp-9-

2891-2009, 2009.

Wang, D. S. and Hildebrandt Ruiz, L.: Secondary organic aerosol from chlorine-initiated oxidation of isoprene, Atmos. Chem. Phys., 17(22), 13491–13508, doi:10.5194/acp-17-13491-2017, 2017.